June 2017

Morphometric Analysis of the Talus on the Cohort of Healthy and Arthritic Patient Population:

Tia Arvaneh
University of South Florida, tarvaneh@gmail.com

Morphometric Analysis of the Talus on the Cohort of Healthy and Arthritic Patient Population: *In-Vivo* 3D Computational Study

by

Tia Arvaneh

A thesis submitted in partial fulfillment
of the requirements for the degree of
Master of Science in Biomedical Engineering
Department of Chemical and Biomedical Engineering
College of Engineering
University of South Florida

Co-Major Professor: William E. Lee III, Ph.D.
Co-Major Professor: Peter Simon, Ph.D.
Stephanie Carey, Ph.D.

Date of Approval:
June 27, 2017

Keywords: Ankle Joint, Osteoarthritis, Computerized Tomography (CT),
Joint Geometry, Talar Dome

DEDICATION

I dedicate this work to my family and friends. Thank you to my parents for the continual love and support, and for teaching me to be confident and fearless.

ACKNOWLEDGMENTS

I would like to extend my gratitude to Dr. Peter Simon for continuous encouragement and support of my research and education. I would also like to thank Dr. William Lee and Dr. Stephanie Carey for their expert involvement and guidance.

TABLE OF CONTENTS

LIST OF TABLES

LIST OF FIGURES

ABSTRACT

Prevalence of osteoarthritis (OA) is less common in the ankle compared to other joints; however, deformation brought on by degeneration causes pain, loss of function, and overall decreased quality of life. Current surgical interventions for end-stage ankle OA are not as reliable as surgical treatments for other joints. Ankle arthroplasty currently has high failure rates, and there are lack of substantial data from long-term outcome studies. By understanding the morphometric changes that occur during the different stages of OA, we are able to identify early signs of the disease with the intention to apply treatment earlier in order to preclude the need for end-stage surgical intervention. The goals of this study are to assess morphometric parameters of the talus as it relates to the progression of OA and to evaluate the effect of gender and anatomical side. A retrospective study was performed where data from sixty-eight CT scans were obtained from two study groups, one with OA and one without. The subjects were segmented, standardized, and normalized in order to study several 3D parameters of the talus, including height, radius of curvature, and volume. Results showed that talar morphometry is influenced by gender and that geometric changes are a function of OA progression. The lateral radii of subjects with OA was significantly larger than those of normal ankles ($p<0.0001$), and there is evidence of inherent changes between KL grades ($p=0.0003$). Identifying morphometric changes of the talus at each stage of OA can inherently contribute to better understanding the degenerative process. Assessing specific characteristics at earlier stages of the diseases may help clinicians to diagnose more accurately and to better provide treatment.

CHAPTER 1: INTRODUCTION

1.1 Study Motivation

An advanced understanding of ankle anatomy and structure is essential for selecting an optimal treatment option for diseased ankle joint, as well as for designing better implants for arthroplasty, especially when aiming to restore natural joint kinematics. The stability and integrity of the ankle joint depends on its congruent articular geometry and ligament attachments. A healthy ankle joint performs basic patterns of motion that are primarily determined by the geometric features of the articulating surfaces of the talus and of the tibia and fibula. Those patterns can be disrupted, commonly by the presence of osteoarthritis (OA), which can be very painful and can affect normal locomotion. This often leads to decreased quality of life in patients because those with ankle OA experience changes in walking mechanics, as well as altered ability to complete many so-called activities of daily living. Any treatment for ankle joint insufficiencies, surgical or nonsurgical, has the goal to repair the joint configuration in order to reproduce close-to-normal movement patterns. Changes in cartilage integrity and articular geometry induced by the presence of the OA may change joint motion, resulting in increased joint restraints (tensioning of ligaments), loss of congruency, or excessive load transfer, which may result in decreased range of motion (ROM).

Ankle OA is diagnosed and graded radiographically by identifying joint-specific morphometric and morphologic features. These features can include joint space narrowing, osteophyte formation and subchondral bone sclerosis. Changes to the talus, including visual

evidence of flattening, can be seen with disease progression. As degeneration affects cartilage, the bone must compensate for deterioration by producing bony growths or by changing bone density. Additionally, effects of talus hypertrophy are noted as they disturb the balance of the ankle's soft tissue. Although not seen in all cases of OA, bony deformation and cartilage degeneration are commonly associated with and may be indicative of joint pain [1].

Little information is known about natural progression of degenerative changes to the ankle caused by OA. Osteoarthritis is generally considered a disease of cartilage degeneration caused by mechanical stress [1]. However, specific characteristics of the ankle's articular cartilage prevent or delay degeneration that commonly appears in OA of the hip or knee. Primary OA is the most common joint disease; though, the majority of cases of ankle OA are due to secondary or posttraumatic causes [2]. Although it occurs less commonly, the pathophysiology of primary ankle OA is still largely unknown [1, 3]. Understanding the pathology of joint degeneration can contribute to algorithms used to designate the optimal forms of diagnostics and treatment. There are various differences between the ankle and the knee and hip that are important to acknowledge when researching etiology. For instance, there are subgroups of ankle OA, including varus or valgus deformities, which influences clinical and radiological characteristics [3].

Previous studies have investigated ankle joint morphometry primarily using 2D x-ray techniques [4]. Subjectivity of such measurements is questionable since their accuracy may be highly dependent on the operator's skill as well as the positioning of the feet during scanning. On the other hand, 3D approaches have been able to offer more adequate descriptions of the ankle joint morphometry in both healthy and diseased states. Using 3D techniques to evaluate the ankle provides an additional dimension and volumetric assessment, which could better describe the conformational changes in the geometry of the joint in situ. Yet, there are only a handful of studies

that have addressed the geometry of diseased ankle joints [5], and even less that have made comparison studies between normal and osteoarthritic joints [6].

1.1.1 Socio-Economic Factors

Osteoarthritis is the most common skeletal disorder, affecting about 15% of the world's adult population [3]. Although it only affects 1% of the population, ankle OA is significantly associated with joint pain, loss of function, decreased ROM, and overall lowered quality of life [1-3]. OA remains ones of the most frequent conditions treated by U.S. hospitals, and is the second most expensive condition [7]. The rising rate of hospitalizations for OA are largely due to the symptomatic effects. Even though OA is graded radiographically, symptoms may appear regardless of physical evidence of degeneration [8, 9]. The majority of clinical costs can be attributed to symptoms such as pain and stiffness because they lead to the need for surgical intervention. Surgical methods tend to be reserved for treatment of end-stage OA because its goal is to restore function that has been altered due to deformity. But, surgical treatments used to reduce or eliminate pain can be used in moderate cases because joint pain can occur even when there is no physical deformations present. Revision surgery may be needed when TAR fails, which overall adds to the cost of treatment as well as symptomatic complications.

The gold standard for surgical treatment is arthrodesis, yet arthroplasty has been increasingly more popular in the last decade due to its more enhanced ability to restore natural movement [9-12]. However, the outcome of Total Ankle Replacement (TAR) has not been as positive as other more established prosthetics, such as Total Knee (TKR) or Total Hip (THR) replacements. Since its introduction and implementation, TAR has had high complication and failure rates [13]. Improvements to the first prosthetic design have been made, but analyses of postoperative outcomes using second-generation TAR are only recently being made available [11,

12]. TAR is generally regarded for treating end-stage OA which may explain why there is a high failure rate because studies have shown that radiographic severity may predict the outcome of arthroplasty [9]. This is why more widespread degeneration that affects the whole joint responds better to arthroplasty [9]. Patients may seek surgical treatments to clinically manage long-term pain and restore motion. More moderate and early-stage cases of OA may not experience as much overall physical degeneration; therefore, arthroplasty and fusion methods will replace or damage healthy areas of the joint as well. Proprioceptive feedback is lost when the joint is replaced, and some patients find this less desirable compared to enduring joint pain if healthy areas remain [3, 9].

Compensation for deterioration to the tissue comes in the form of alterations to the bone, including osteophyte formation, bony spurs, and overall enlargement of the talus [1, 14, 15]. Bone alterations contribute to the pain associated with OA. Changes in bone occur in tandem to the progress of degeneration. Although the etiology has yet to be proven, there is a strong relevance between ankle OA and changes in bone which contribute to its pathophysiology. The goal of OA treatment, besides decreasing long-term pain, should be to lessen the progress of the destruction of the bone. Diagnosing OA radiographically at earlier stages can contribute to this goal. Radiographs are more widely used for OA imaging due to extensive availability and lower costs compared to MRI and CT imaging. But, the advantage of using MRI and CT over X-rays is that information regarding the progression OA can be revealed by the enhancement of surrounding tissues as well as bone [8, 16]. Cartilage degeneration may provide additional information regarding the progression of OA because inflammatory episodes can be linked to disorder of the cartilage matrix [17].

1.2 Study Aims

The goal of this study is to develop a methodology for in-vivo quantification of the 3D geometry of the talus; and to assess the geometric parameters of the talus on the cohort of healthy and diseased patients. These parameters will be evaluated against gender, side, and degree of OA progression. We hypothesize that changes to the size and shape of the talus are a function of OA progression, as reflected by Kellgren-Lawrence (KL) grade.

1.3 Innovation

Progress in clinical imaging technology and ever-widening access to advanced imaging modalities enable clinicians and scientist to visualize and evaluate shape and condition of the human anatomy with great precision. Consequentially, geometric-based, objective parameters of healthy and pathologic anatomy can be easily derived from these high-resolution imaging modalities, and can be further used to describe morphometry and morphology of anatomical entities. Previous studies have evaluated the two-dimensional and three-dimensional geometry of healthy [4, 5, 18-21] and arthritic ankle joint at the end-stage OA [6]. Despite a volume of gathered information, the 3D quantification of talar geometry as a function of the OA progression remains elusive.

The primary goal of this thesis was to develop analytical tools and techniques capable of extracting clinically meaningful 3D information on the morphometry obtained from 3D point-cloud data (clinical CT). In order to achieve this goal, the following criteria have been established:

- Only a 3D approach to morphology analysis will be utilized.
- All proposed methods are free of identification of distinct anatomical landmarks that may be particularly difficult to recognize in arthritic patients. Rather, all methods are automatic, based on subject-specific geometry.

- Every step of the process carrying operator bias will follow a standardized procedure.
- Models of the human anatomy and all performed measurements will be subject-specific.

CHAPTER 2: HUMAN ANKLE BACKGROUND

2.1 Ankle Joint Anatomy and Structure

The ankle refers to a complex structure of the subtalar, talocrural, and talocalcaneonavicular joints (Figure 1) [22]. The load-bearing aspect of the ankle occurs at the interface where the tibia meets the talus [22]. Located at the distal ends of the tibia and fibula, the talus works in articulation to form the diarthrodial talocrural joint [22, 23]. The talus can be subdivided into the head, neck, and body, and is supported by joint capsules, ligaments, and synovial tissues (Figure 2). It has no muscular attachments. It is suggested that the unique geometry of the talus, along with surrounding tissue, contributes to the stability of the joint. The majority of the talar surface is covered by articular cartilage.

2.1.1 Talus Structure

The talar head has four articular surfaces. The large, convex anterior surface interacts with the navicular bone (Figure 1). The inferior surface is composed of two facets separated by smooth ridges. The medial and lateral surfaces interact with the calcaneonavicular ligament and the calcaneus, respectively.

The neck, lying between the talar head and body, presents itself as an area to which ligaments attach. It contains a deep sulcus, which forms the roof the sinus tarsi when involved with the articulation of the talus and the calcaneus. The sinus is a small cavity that contains the interosseous talocalcaneal ligament and the joint capsule.

The body makes up the majority of the talus, and has more prominent articular surfaces compared to the neck and the head. It is superiorly covered by a trochlear surface, which is also known as the talar dome. The trochlea articulates with the distal end of the tibia and is wider anteriorly. The medial and lateral aspects of the trochlea exhibit different radial curvature. The medial surface presents a facet for the medial malleolus, and it is continuous with the trochlea. The lateral surface, similar to the medial surface, contains a facet for the lateral malleolus, but only its anterior half is continuous with the trochlea. The lateral portion forms a triangular facet that is in contact with the transverse inferior tibiofibular ligament during flexion. The rough posterior surface contains a groove specified for the tendon of the flexor hallucis longus.

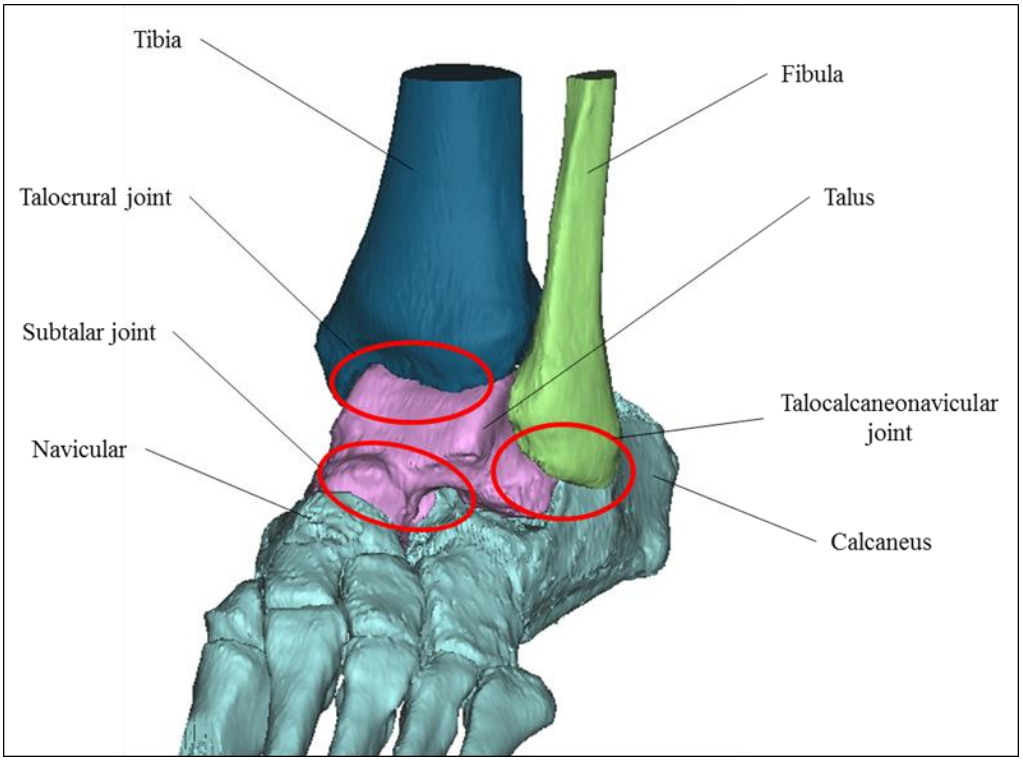

Figure 1 Basic structure of joints of the ankle complex.

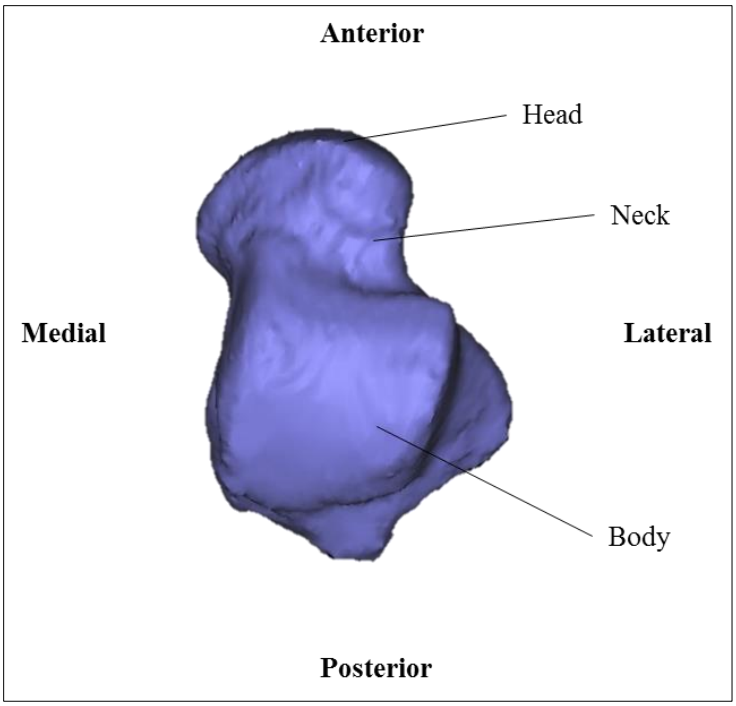

Figure 2 Superior view of the talus depicting the head, neck, and body.

2.1.2 Articulating Surfaces

The three articulating surfaces of the ankle are the malleolar mortise, the trochlea of the talus, and the malleoli of the tibia (Figure 3). The malleolar mortise is formed by the distal ends of the tibia and the fibula and is strengthened by the interosseous membrane and tibiofibular ligaments. The mortise fits with the trochlea, which is shaped like a pulley. The tibia transfers body weight to the talus when it articulates with the roof the malleolar mortise. Additionally, the medial malleolus of the tibia interacts with the talus while the lateral malleolus is located on the outer surface of the ankle. The malleoli are responsible for gripping onto the talus during ankle movement and flexion. Since the malleoli constrain the talus, they strongly influence the joint function. This interaction is strongest during dorsiflexion because the anterior end of the trochlea is wider, forming a tighter grip as the bones become more packed. This also causes slight spreading

of the mortise. The ankle becomes less stable during plantarflexion because the narrower end of the trochlea causes loosening within in the mortise.

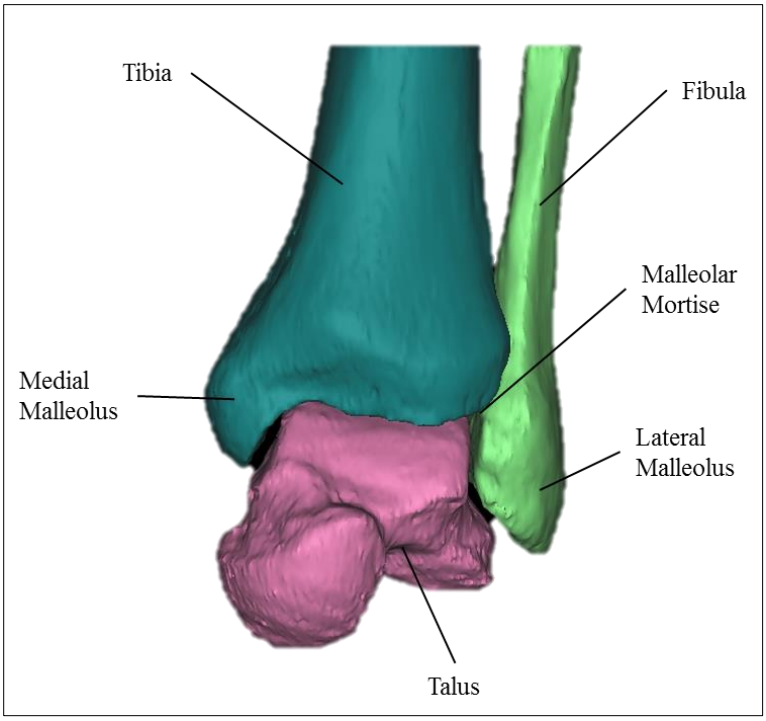

Figure 3 Skeletal anatomy and articulating areas of the talocrural joint.

2.1.3 Functional Anatomy

The ankle functions as a rolling joint and mainly allows for dorsiflexion and plantarflexion movements [3, 22, 24]. Small amounts of abduction, adduction, inversion, and eversion are possible due to the loosening of the trochlea during plantarflexion. Through the compilation of all joints of the complex, the ankle motions consist of plantar- and dorsiflexion in the sagittal plane, ab- and adduction in the transverse plane, and inversion and eversion in the frontal plane [22]. Supination and pronation of the foot are caused by simultaneous movements in all three planes [22, 25].

2.1.4 Articular Cartilage and Loading

Articular cartilage covers surface of the ankle and is mainly responsible for the unique biomechanical properties of the joint. Ankle cartilage has specific properties which makes it unique compared to articular cartilage of other weight-bearing joints, such as the knee. The talocrural joint is highly congruent, but ultimately its congruency is variable and dependent on the motion of the foot and ankle and amount of load [14, 17, 24]. When lighter loads bear on the ankle, there are incomplete and separate contact areas. The joint transitions to complete congruency during activity and when bearing higher loads, allowing it withstand larger pressures [3, 22]. The load-bearing area of the ankle is small and consequently experiences more force per area. Load exhibited on the ankle can range from 1.5 to 7 times body weight, depending on level of activity [13, 26, 27]. The joint contact area averages 300 mm^2, whereas the knee and hip are about 1,120 mm^2 and 1,100 mm^2, respectively [2, 3, 13, 22]. Ankle cartilage is uniform and thinner than other joints in the lower extremity. The average thickness in healthy ankles measures between 1 and 1.7 mm, whereas the knee joint varies between 1 and 6 mm [14, 24, 28]. It has been hypothesized that congruent joints, such as the ankle, are covered by thin cartilage because the compressive loads are spread over a wider area [27]. This reduces and eliminates local joint stresses and large cartilaginous deformations. Joints covered by thicker cartilage experience increased load-bearing area when the cartilage begins to deform [29]. A more resistant cartilage could explain why the ankle is less susceptible to degenerative changes caused by primary osteoarthritis.

The biochemical characteristics of ankle cartilage also play a large role in its resistance to degenerative changes. Cartilage consists of chondrocytes, which are cells that produce and maintain the cartilaginous matrix [17, 27, 28, 30]. The matrix consists of collagen, hyaluronic acid, proteoglycans, and a small number of glycoproteins, and can be subdivided into the superficial,

radial, deep, and calcified zones [24, 27, 28]. Chondrocytes synthesize and turnover a large number of these components, which is a crucial property that leads to maintenance of the matrix [28, 30]. Proteoglycans exhibit significant turnover throughout life, whereas collagen has a much longer turnover span [17, 24, 30]. Chondrocytes respond to outside stimuli and tissues damage, and are also responsible for degenerative conditions. Elasticity of the cartilage is dependent on the electrostatic connections between collagen fibers and the glycosaminoglycan (GAG) side chains of the proteoglycans [3, 24, 27, 30]. The GAG side chains also play a vital role in maintaining water content of cartilage. The ankle has a significantly higher GAG content and lower water content, which could contribute to its higher compressive stiffness and lower hydraulic permeability [17, 27].

Chondrocytes are responsible for upregulating proteinase activity, which has been observed to contribute to loss of proteoglycan in the cartilage of other joints [30]. A previous study tested this metabolic property and observed negligible loss of cartilage proteoglycan in the ankle, suggesting that there is more activity in regards to both synthesizing and degrading proteoglycans [17]. The ankle is also less responsive to catabolic stimulation compared to other joints, like the knee. Interleukin-1β is a pro-inflammatory catabolic cytokine. At high concentrations, it is effective in stimulating proteolytic enzyme synthesis and degrading components of the extracellular matrix. It has the ability to inhibit synthesis of proteoglycans in chondrocytes. However, this response is weak in the ankle possibly due the number or types of IL-1 receptors [17, 27, 30].

2.2 Pathology and Clinical Significance

Compared to other joints in the lower extremity, the ankle is far less susceptible to degenerative processes such as osteoarthritis. OA appears substantially less in the cases of the

ankle because of unique anatomic, biochemical, and cartilage characteristics. The most common cause of ankle OA stems from posttraumatic origin, unlike the appearance of primary OA in most other joints [2, 3]. Pathologic conditions might be caused by acute or chronic mechanical overloading, systemic mal-loading, or habitual under loading leading to disuse atrophy [3, 31].

2.3 Ankle Osteoarthritis

Although osteoarthritis is a frequently occurring degenerative joint disease, OA less commonly appears in the ankle. Osteoarthritic diseases have mechanical and biological causes and result in progressive degradation of articular cartilage and subchondral bone. Degeneration can further be aided by osteophyte formation, subchondral bone sclerosis, bone marrow lesions, and synovial membrane inflammation [3, 8, 14-16]. OA is characterized by joint pain, tenderness, loss of motion and function, and various degrees of inflammation. Risk factors for OA include age, obesity, metabolic disease, abnormal mechanics, joint malalignment, and joint trauma [31, 32]. OA can affect both men and women, but there is increased risk in post-menopausal women due to changes in joint metabolism [33]. Primary osteoarthritis has idiopathic origins, and the most commonly occurs in the hip and knee. On the other hand, ankle OA can largely be attributed to secondary causes and is most often a result of traumatic injury. Injuries that may result in OA include fractures of the malleoli, tibial plafond, talus, isolated osteochondral damage of the talar dome, and ankle ligament injury [3, 31].

The intermittent inflammatory response of OA is due the disorder of cartilage matrix metabolism controlled by chondrocytes. When the articular cartilage is damaged, the extracellular matrix is lost, which leads to chondrocytes attempting reparation. However, the turnover rates of the components of chondrocytes are not balanced and result in slow progression of degeneration [27, 30]. Proteoglycan decreases overtime, allowing the cartilage to eventually become more

susceptible to changes caused by mechanical stress. The upregulation of inflammatory cytokines and metalloproteinases lead to the disruption of the cartilage homeostasis and contribute to matrix degradation [28, 30]. However, as previously mentioned, ankle cartilage is not as vulnerable to these catabolic changes.

Excessive mechanical loading is also known to cause cartilage degeneration. When there is an imbalance, as seen with posttraumatic injuries and instability, the cartilage cannot sufficiently protect the joint from additional forces. Normally, mechanical forces stimulate chondrocytes and activate mechanoreceptors [30]. This leads to the activation of regulatory molecules and intracellular signaling cascades, whose goal is to change gene expression and protein production [30]. Through this signaling mechanism, an anabolic response is elicited to maintain the cartilage. Mechanical overloading causes a homeostatic shift in the tissue remodeling factor, which results in catabolic activity [29].

Although the etiology of osteoarthritis is still largely unknown, the ankle exhibits unique biomechanical, biochemical, and metabolic properties that allows it to be less prone to the disorder. The ankle cartilage's resistant properties mainly contributes to the rarity of OA formation, particularly because of the high biochemical influence of degenerative changes.

2.3.1 Methods of Diagnosis

Osteoarthritis can be identified radiographically, clinically, or symptomatically. Ankle OA is most commonly diagnosed and graded radiographically by identifying joint specific morphometric and morphologic features. Defining features of OA include osteophyte formation, joint space narrowing, sclerosis, cysts, and deformity [7, 8, 14]. These features are identified on x-ray images and classified based on the standardized Kellgren-Lawrence (KL) scale (Table 1) [8]. OA is typically defined as a KL grade of 2 or higher [7].

The KL scale could be regarded as disadvantageous because it implies that the progression of the disease is linear. Another oversimplification of using the KL classification is the dependence on osteophyte formation. OA progression does not always include the formation of osteophytes or the inclusion of cartilage degeneration. Structural changes of the ankle due to OA may occur before it is radiographically present [14]. Those who are regarded as KL grade 1 are identified as being non-pathologic, however, the features at this grade may be regarded as early signs of the disease.

Other imaging modalities are more frequently being used in the process of OA diagnosis. Magnetic resonance imaging (MRI) provides greater information regarding surrounding soft tissue structures [34]. More information regarding disease progression can be revealed by MRI imaging because it may assess articular cartilage, osteophytes, subchondral bone, and ligamentous and synovial structures using both qualitative and quantitative methods [8]. Similarly to using MRI, computed tomography (CT) imaging can reveal the degree of soft tissue involvement. CT is commonly utilized for postoperative assessment [34].

Symptomatic OA is defined by the combination of prevalent symptoms in addition to radiographic features. Common identifiable symptoms of ankle OA are pain and stiffness. The prevalence of pain is associated with more severe cases of OA. There are incidences where radiographic evidence is present but symptoms are not, and vice versa [7].

Table 1 Kellgren-Lawrence radiographic classification for osteoarthritis.

Grade	**Classification**	**Description**
0	Normal	No radiographic features of osteoarthritis
1	Doubtful	Possible osteophytes, doubtful joint space narrowing
2	Minimal	Definite osteophytes, possible joint space narrowing

Table 1 (Continued)

3	Moderate	Definite narrowing of joint space, moderate multiple osteophytes
4	Severe	Joint space greatly impaired with sclerosis of subchondral bone, definite deformity of bone ends

2.3.2 Surgical Treatment

The goal of surgical intervention for ankle osteoarthritis is to relieve pain long term and to attempt to regain as much natural motion as possible. Current surgical options are limited to arthroplasty, or joint replacement, and arthrodesis, or fusion surgery.

The current gold standard for arthritis is arthrodesis [13, 35, 36]. The goal of arthrodesis is to fuse two or more bones together to form one compressive unit. Hardware is used to constrain the bones together. Ankle arthrodesis can be categorized by the condition of the ankle. An open technique is necessary to obtain re-alignment of deformed ankles [35]. Arthritic ankles with relatively good alignment can be manipulated by fusion in situ. In the ankle joint, the tibia and fibula are designated to be fused by compression and fixation. Pain relief is seen with a lot of patients post-operatively, but loss of motion is compromised [12, 13, 35, 37, 38]. Long-term problems may arise from arthrodesis. With decreased function of the ankle, increased contact stress and force are applied to neighboring joints, ironically leading to the possibility of arthritic degeneration [13, 35, 37].

Due to long-term problems caused by arthrodesis, Total Ankle Replacement, commonly known as arthroplasty, was introduced as a motion-preserving alternative [12, 13]. TAR may be beneficial for patients who already have degeneration in surrounding joints because arthrodesis risks increasing degeneration due to shifts in abnormal loads [13, 39]. The biomechanics and unique geometry involved with the ankle joint pose as a challenge for the design and

implementation of arthroplasty. Because the axis of rotation is inconsistent during movement, a component design must take into account that there are multiple rotational forces. First-generation prosthesis models were highly constrained which caused excessive transfer of shear, compressive, and rotatory forces to the ankle [13, 24]. A semi-constrained model was implemented to address multi-force motion. As seen with the issues from the first-generation design, reducing constraint minimizes spread of shear forces as the bone interface [12, 13, 39]. One prosthetic design contains a tibial and a talar component which functions as a ball-and-socket configuration. This design allows for some sliding and rotational motion. A three-component design, consisting of a metal tibial plate, a metal talar component, and a polyethylene bearing, allows for more movement. Flexion and extension occurs at the talopolyethylene interface, and internal and external rotation and translation occurs at the frontal and sagittal planes of the tibiopolyethylene interface [39]. All current prosthetic models are stabilized by bone ingrowth. This requires less bone resection and allows the implant to avoid damage to local soft tissues and bony surfaces.

Functional outcomes have been reported with the new design of TAR. However, there are still problems that results in high failure rates. Imbalance of surrounding soft tissue as well as bony growth development or deformity may affect survival of implantation [12, 13]. These problems could lead to malalignment, loosening, and component failure [12, 13].

2.4 Summary of Literature Review

For an overview of parametric outcomes from the following studies, refer to Appendix B. The following studies are separated by study group, starting with studies that included osteoarthritic subjects, followed by studies that excluded pathology from their subject groups.

Wiewiorski et al. [6] is the only study out of the review that evaluated morphometry in both osteoarthritic and non-diseased ankles using 3D models. Reference planes were used for

measurements of the talus and the distal tibia. Sagittal planes were applied at the center, medial, and lateral portions of the talus. In each of the sagittal planes, five points that lied along the talar dome surface were selected. A circle was automatically fit to these points, and the radius of the circle was calculated. While still using anatomical planes as reference points, the height of the talar dome was measured as the difference between the transverse plane and the highest points of the medial and lateral edges.

Hayes et al. [5] conducted a study using CT images from patients who were diagnosed with unilateral osteoarthritis. Unlike the study done by Wiewiorski et al., Hayes et al. did not produce 3D models but instead used the CT images to make on-display measurements. Calculations were dependent on the operator's skill. A local coordinate system was produced from reference planes based on anatomical landmarks of the talus. The transverse plane was defined as a plane parallel to both the tangential line of the superior surface and the line passing through the anterior and posterior ends of the talar dome surface. The radius of the arc of the talar dome was digitally calculated from three surface points that lied on the anterior, middle, and superior portions of the talar dome surface. The radius was reported as being the midsagittal radius of the talar dome. The parameter was evaluated against gender.

In a previous study also conducted by Wiewiorski et al. [21], the upper articular surface of the talus was reconstructed and evaluated by using 564 CT images of the ankle. The study excluded any subjects showing pathology, which resulted in a remainder of 83 images that were used for analysis. In a similar approach to their 2016 study, the measurements of the talus were done with respect to anatomical reference planes. The medial and lateral edges were identified by adjusting a frontal plane by 30 degrees anteriorly and posteriorly. Five points were selected along the talar dome, which then a circle was fitted to represent sagittal curves. A unique parameter, known as

the talar dome ratio (TDR), was introduced. The TDR was calculated as a ratio between the line connecting the highest points of the medial and lateral talar edge and the distance between that line and the deepest point of the talar sulcus. While TDR was used to assess the correlation between the concavities of the talar dome and age groups, Wiewiorski et al. found no statistical differences.

Siegler et al. [20] took at an approach toward the morphology of the ankle as it related to the findings of Inman. The study took CT data from 26 healthy ankles and created 3D representations used for analysis. Several contours were fitted to the talar models based on several facets. The facets were created based on an initial medial sagittal section, which was manually selected. To measure the radii of curvature, circles were fitted to the contours of the facets in the least-square errors sense. The contour of the trochlea was included within the anterior and posterior boundaries.

Kuo et al. [19] tested a total of 31 morphological parameters using 3D geometric models reconstructed from CT images of 58 cadaver ankle specimens. The specimens used were obtained from patients who underwent amputation for reasons other than trauma or disease of the ankle joint. Of the 31 parameters, 18 were for the talus and 13 were for the tibia and fibula segment. Measurements were taken based on an embedded global coordinate system with the origin at the geometric center of the talus. In the talar interface, they measured medial and lateral trochlea tali length, center, anterior, and posterior trochlea tali width, central, medial, and lateral tali radius, and talar cross-sectional area, as well as ratios between arch length and width. Parameters were evaluated against gender.

Stagni et al. [4] used a 2D-based method to evaluate geometry of the ankle. X-ray pictures were obtained from 36 subjects while in unloaded conditions. An operator was used to make initial reference marks which was then analyzed by software for more complex measurements. By

initially identifying points on the talar dome, a circle was fit to these point in order to calculate the radius of curvature. Results were compared between genders.

CHAPTER 3: MORPHOMETRY OF THE ANKLE JOINT

3.1 Study Population

A total of 68 ankles were included in this study. Pre-operative imaging data was obtained from the database of the affiliated orthopaedic hospital. All patient information was blinded and only gender, age, and anatomical side were retrospectively collected. Inclusion criteria were subjects older than 18 years of age, no talus fracture/previous talus surgery, no rheumatoid arthritis, existence of the CT scan with entire talus in the field of view, and absence of any metal in the field of view (anchors, screws, wire, etc.). An orthopaedic resident with professional interest in ankle trauma evaluated all imaging and clinical information to determine KL grade and inclusion in this study. All patients included had ankle computer tomography (CT) scans previously done following standardized protocol: slice thickness 1.25 mm, field-of-view approximately 10 cm, entire talus bone in the field of view, imaging taken on the same CT scanner - GE Lightspeed QZ/i Helical Scanner (GE Healthcare, Waukesha, WI, USA). The images were stored in Digital Imaging and Communications in Medicine (DICOM) format and then transferred to computers for analysis.

The study population of 68 ankles consisted of 23 ankles that were considered healthy and 45 ankles that had been diagnosed as arthritic, with a KL grade of 2, 3 or 4. There were 29 females and 39 males, and 28 of the images consisted of left ankles while 40 images were of right ankles. The average age was 59±17.3 years (range 18-84 years), 44.8±17.2 (range 18-74 years) in the healthy group and 66.6±12.1 (range 24-84 years) in the OA group. The OA group consisted of the following: 22 subjects graded KL 1 (12 males, 11 females), 4 subjects graded KL 2 (3 males, 1

female), 27 subjects graded KL 3 (18 males, 9 females), and 14 subjects graded KL 4 (5 males, 9 females).

3.2 Methodology

3.2.1 Segmentation, Standardization, and Normalization

3.2.1.1 Segmentation

3D models of the talus were created using MIMICS v14 (Materialise, Luven, Belgium) following a standardized protocol (Appendix A.1) by a single operator. CT image data was imported originally in DICOM format to the segmentation software (MIMICS). Based on the visual observation, the value of the Hounsfield Unit (HU) representing the cortical shell of the talus was selected as a threshold level to define the cutoff between soft tissue and bone. Once entire talar bone was segmented and transformed into 3D model, one text file containing coordinates of the outer shell corresponding to the talar cortex and another separate text file containing coordinates of the talar volume were exported. To determine the talar dome surface area, a custom-written software was utilized. The talar dome surface was manually extracted from the talus model following a standardized protocol (Appendix A.2) by a single operator.

Any analysis performed past this point was free of operator bias – only custom-written fully-automatic algorithms (MATLAB, MathWorks, Natick, MA) were used for the remainder of the subsequent analysis.

3.2.1.2 Standardization

In order to create a uniform coordinate reference system for every individual talus, a previously created model representing the point-cloud model of the talar dome was utilized. A set of three orthogonal, principal eigenvectors representing the orientation of the studied entities were calculated using the power method for principal component analysis (PCA). PCA orthogonally

transforms a large dataset by identifying a smaller number of uncorrelated variables. It explains the maximum amount of variance with the fewest number of principal components, or eigenvectors. Every eigenvector has a corresponding eigenvalue, which is the magnitude of variance in the data in that eigenvalue's direction. The principal component, is the eigenvector with the highest eigenvalue, and points in the direction of greatest variance in the dataset. The second eigenvector points in the direction of greatest variance of data orthogonal to the first. The last eigenvector points in the direction with the least amount of variance. In the model used, the first eigenvector was approximately in the mediolateral direction, or the x-axis. The second eigenvector was approximately in the anteroposterior direction, or the y-axis. Lastly, the third eigenvector was in the longitudinal direction, or the z-axis (Figure 4a).

Using orthogonal transformation, every talus model was converted from a global coordinate system established by the CT into a new local coordinate system established by applying PCA (Figure 4). The geometric center of the talus was set at local coordinate system with the center of the talar dome located at [0,0,0]. The models were first translated so that the geometric center was located at the origin, then they were rotated to the new local axes. The three components constituting orthogonal subject-specific coordinate system were aligned with the axes of the local coordinate system (Figure 4b).

All models were then adjusted to uniformly represent the same anatomical side. Analysis was done according to the talus on the left leg. All models whose original orientation was not left-sided were adjusted by inverting the x-axis to reflect the standard orientation (Figure 5).

3.2.1.3 Normalization

Before analyzing morphological parameters, all subjects were normalized using the transverse plane of the talar dome surface. To create a transverse plane, four points representing

the talar dome were obtained. A minimum bounding box was applied to the talar dome in order to calculate the smallest dimensional values. The box was then segmented with respect to its length on the x-axis. The length was divided to create fifty slices perpendicular to the mediolateral axis. The most anterior point was identified for each slice. Overall, fifty points were compiled and identified as the anterior points of the talar dome. To account for outliers, points outside of the 95th percentile were removed. The same process was done to obtain the most posterior points of each slice, obtaining a set of the posterior points of the talar dome. The most medial and lateral points were respectively attained from these two sets and used to fit the source transverse plane (Figure 6a,b). A target transverse plane was creating using the same center point from the source transverse plane (Figure 6c,d). All the points both talus models were transformed from the source plane to the target plane.

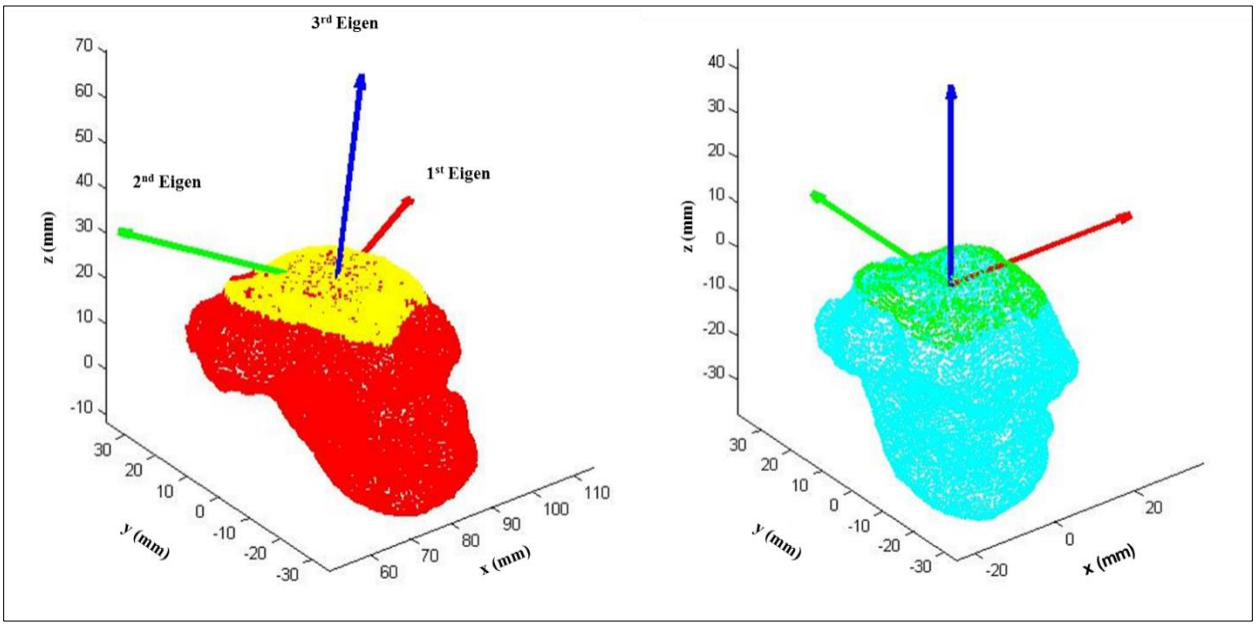

Figure 4 Principal Component Analysis applied to the model of the talus. a) First three components calculated on the talar model in the original global coordinate system. b) Talar model transformed to new local coordinate system.

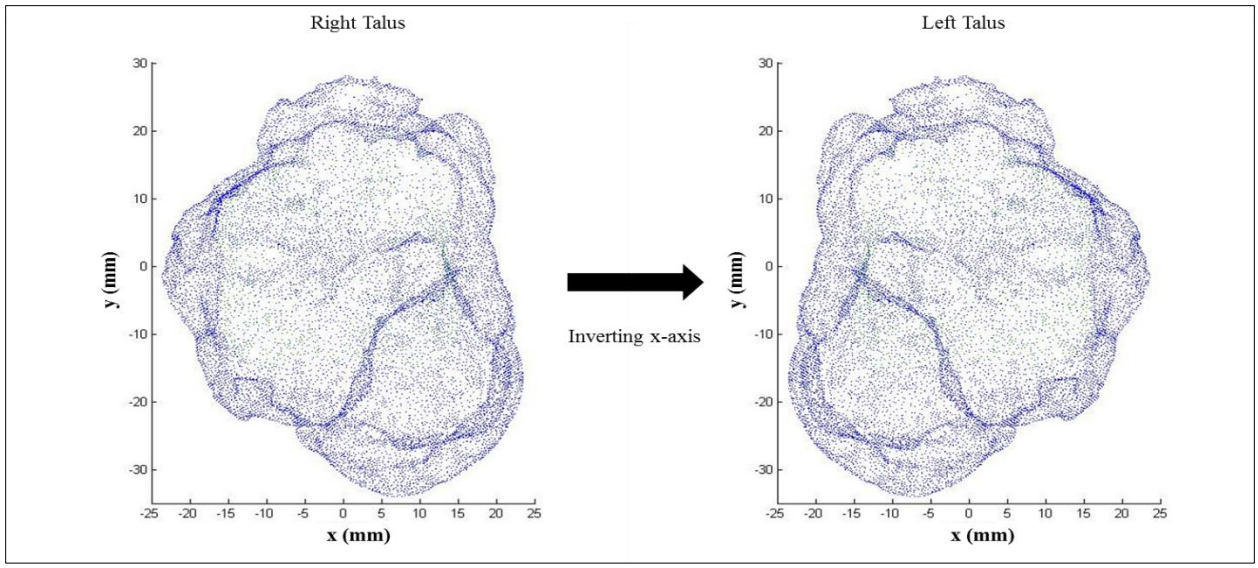

Figure 5 Re-orienting right sided ankles to reflect the left side by inverting the x-axis.

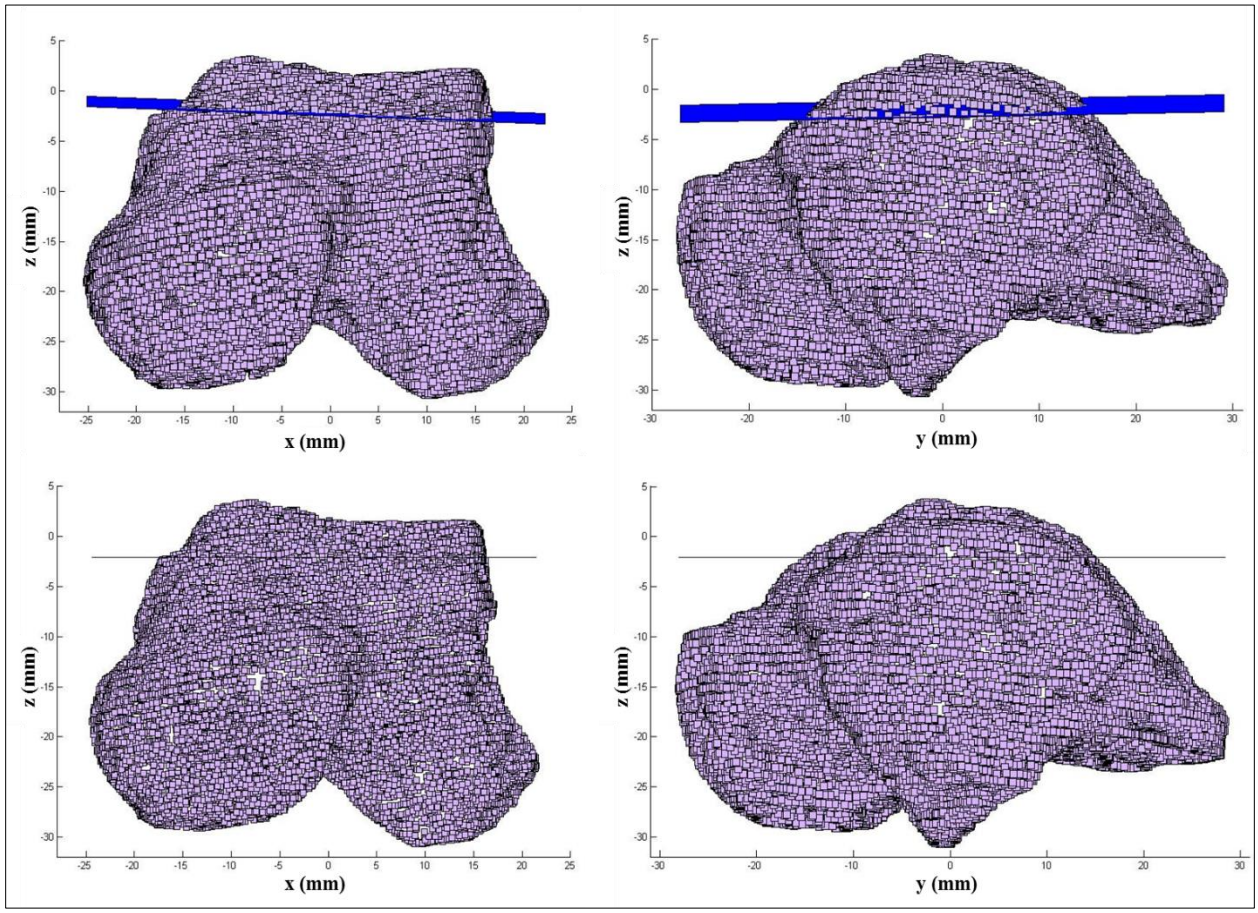

Figure 6 Transformation of transverse plane of the talar dome. a) Anterior view of the talus before transformation. b) Medial view of the talus before transformation. c) Anterior view of transformed talus. d) Medial view of transformed talus.

3.2.2 Medial and Lateral Apex Calculation

The talar dome was separated into its respective medial and lateral regions. All points were first sorted in ascending ordering with respect to the x-axis in order to design all calculations based on the anterior view of the talus. The median point of the dataset was chosen as the midpoint reference. Since all of the models were oriented to reflect the left ankle, all points to the left of the midpoint corresponded to the medial side, and all points to the right of the midpoint corresponded to the lateral side.

The medial and lateral apexes were used as reference points for calculating morphological parameters. Before identifying its apex, the medial surface was divided into 1 mm sections. Within in each section, the most superior point within that range was obtained. This was done for every section until all the points within the medial surface were accounted for (Figure 7). To find the apex, a process was created to evaluate a point against the former and subsequent points. Starting from the outermost point moving toward the midpoint, each point was assessed based on its position with respect to longitudinal height. If a point is lower on the z-axis compared to the location of the next point, then the sequence continues. Once the sequence encounters a point that is higher than both its former and subsequent neighbors, it will stop and designate that point as the apex. The same process was done for the lateral portion of the talar dome to obtain the lateral apex.

3.2.3 Study Parameters

The main study parameters included in this current study were medial and lateral height and medial and lateral radius of curvature. Calculations of both height and radius of curvature were done with respect to the entire talus using the medial and lateral apexes as reference points.

Height and radius of curvature were measured for both medial and lateral sides of the talus. The medial and lateral heights were measured using similar but disparate methods. Before

calculations, the talus was separated into its respective medial and lateral portions, similar to sectioning the talar dome, by creating a midsagittal plane (Figure 8). Using the medial portion of the talus, two sets of points were identified: the most posterior points of the entire talus and the inferior points along the talar head. A plane was then fitted to these points. The medial height was calculated as the Euclidean distance between the medial apex and this plane (Figure 9). The lateral height of the talus was calculated as the distance between the lateral apex and the lateral process. Before identifying the lateral process, the talar model was condensed to reflect the talar body only. Observing the lateral portion only, the lateral process was visually identified as the most plantar point in the [y,z] plane. A transverse plane was anchored at the lateral process, and the height was calculated as the Euclidean distance between the lateral apex and this plane (Figure 10).

The radius of curvature of the talar dome was calculated from medial and lateral facets of the talus, where the apexes were used as reference points. To create the facets, surface-fitting sagittal planes were defined at the location of the apexes. At each apex point, a 0.5 mm range was defined on the x-axis. All points that were within this range were extracted for further analysis (Figure 11). The convex hull of these points was calculated in the [y,z] plane (Figure 12). The polygonal area of this convex hull was calculated and made equivalent to the area of a circle in order to find the radius of curvature. The medial (1) and lateral (2) talar radii were calculated by applying this equation (Figure 13).

$$medial\ radius\ = \sqrt{\frac{medial\ polygonal\ area}{\pi}} \quad (1)$$

$$lateral\ radius\ = \sqrt{\frac{lateral\ polygonal\ area}{\pi}} \quad (2)$$

3.2.4 Other Parameters

Novel parameters measured are the volume of the talar body and the talus using a cylindrical shape and a truncated cone shape. Cylindrical and truncated cone volumes were calculated for the talar body and the talus. For measurements using the entire talar model, a minimum bounding box was applied to obtain the smallest volumetric dimensions of the talus. The length along the x-axis of the box was used as the length 'L' for calculations (3) (4). The length of the talar body was measured as the mediolateral length of the minimum bounding box of the talar dome. The lateral radius 'r_L' was used as the uniform radius in calculations of the cylindrical volume (3) (Figure 14). Both the medial radius 'r_M' and the lateral radius 'r_L' were used in calculations for the truncated cone volume (4) (Figure 15).

$$cylindrical\ volume = \pi * r_L^2 * L \quad (3)$$

$$truncated\ cone\ volume = \frac{1}{3} * \pi * L * [r_M^2 + r_L^2 + (r_M * r_L)] \quad (4)$$

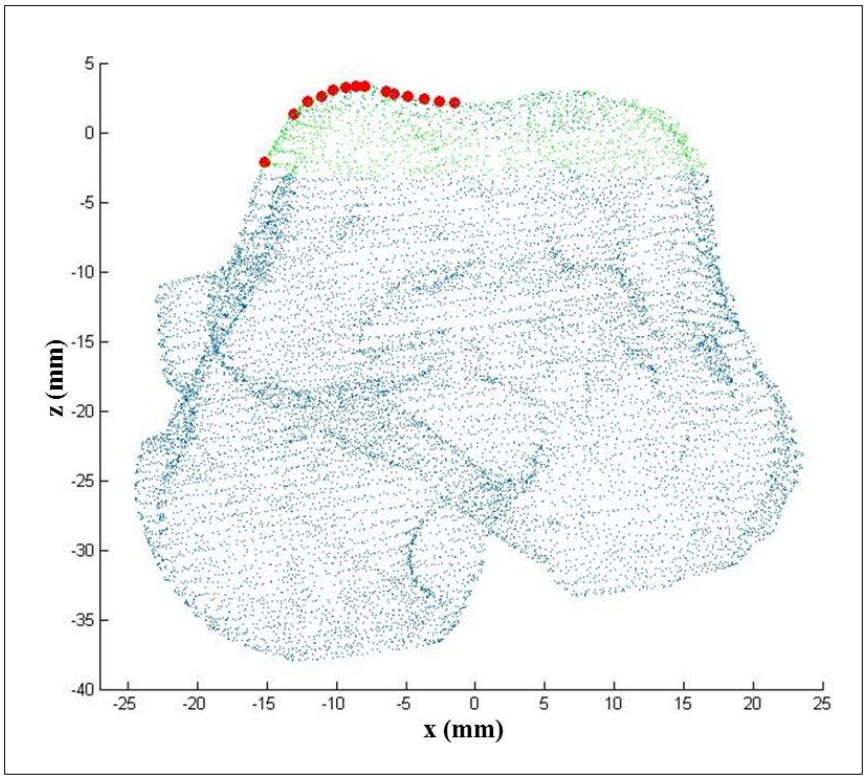

Figure 7 Identification of the most superior points of the medial side of the talar dome surface.

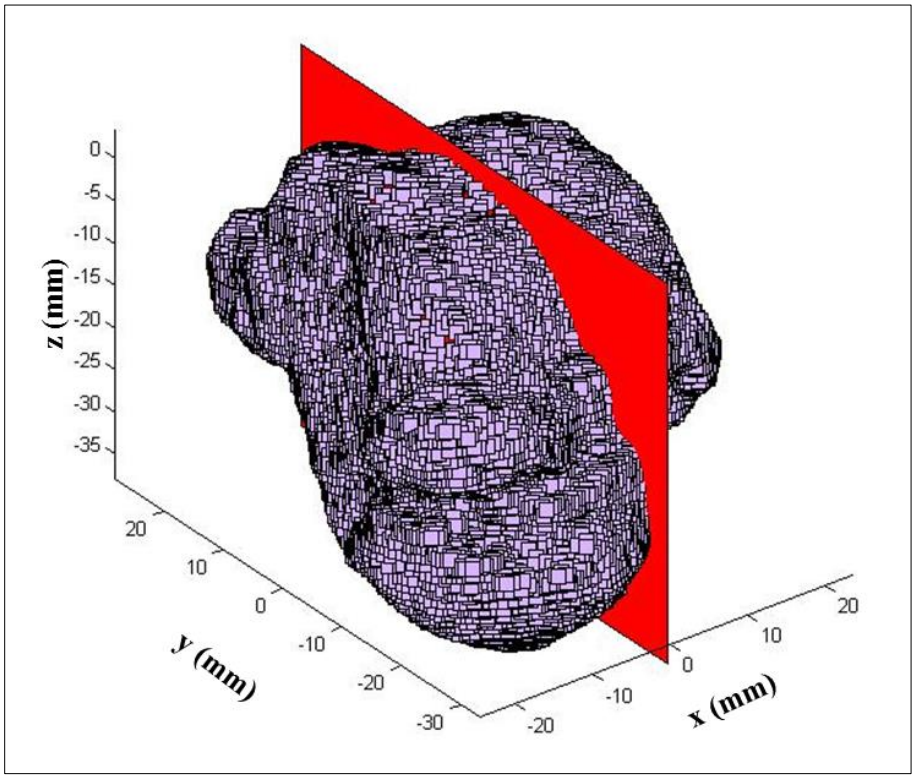

Figure 8 Midsagittal plane applied to the talar model.

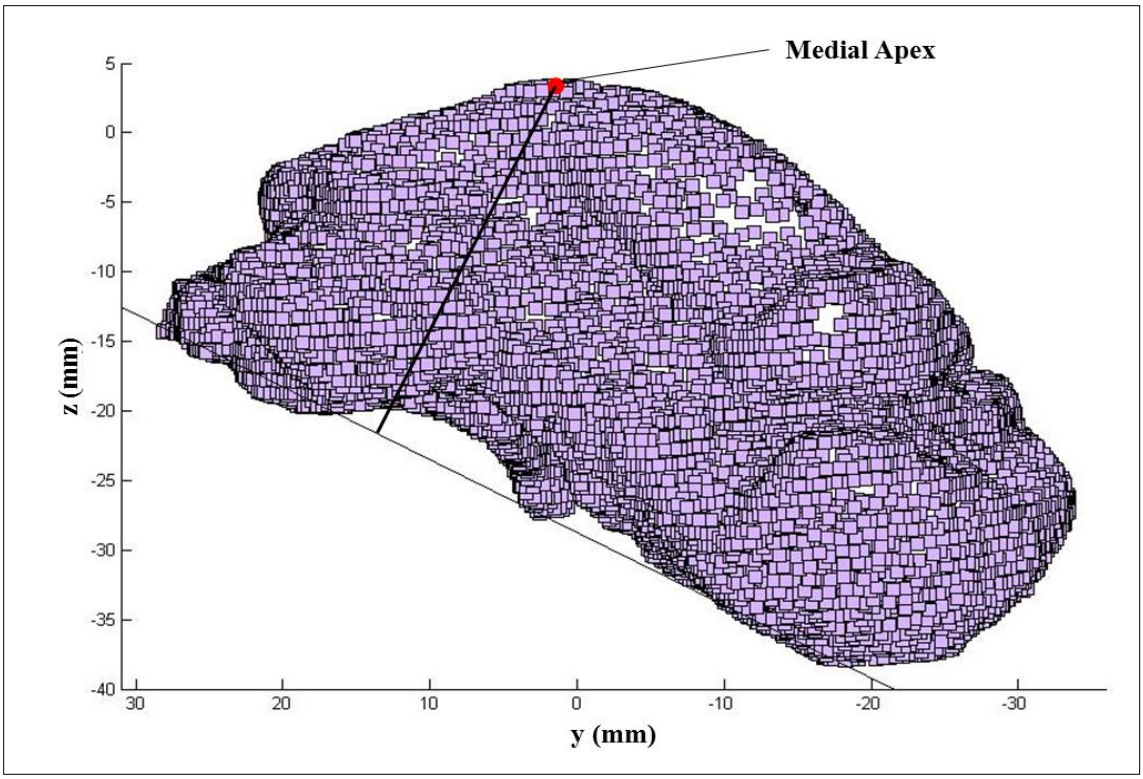

Figure 9 Calculation of the medial height.

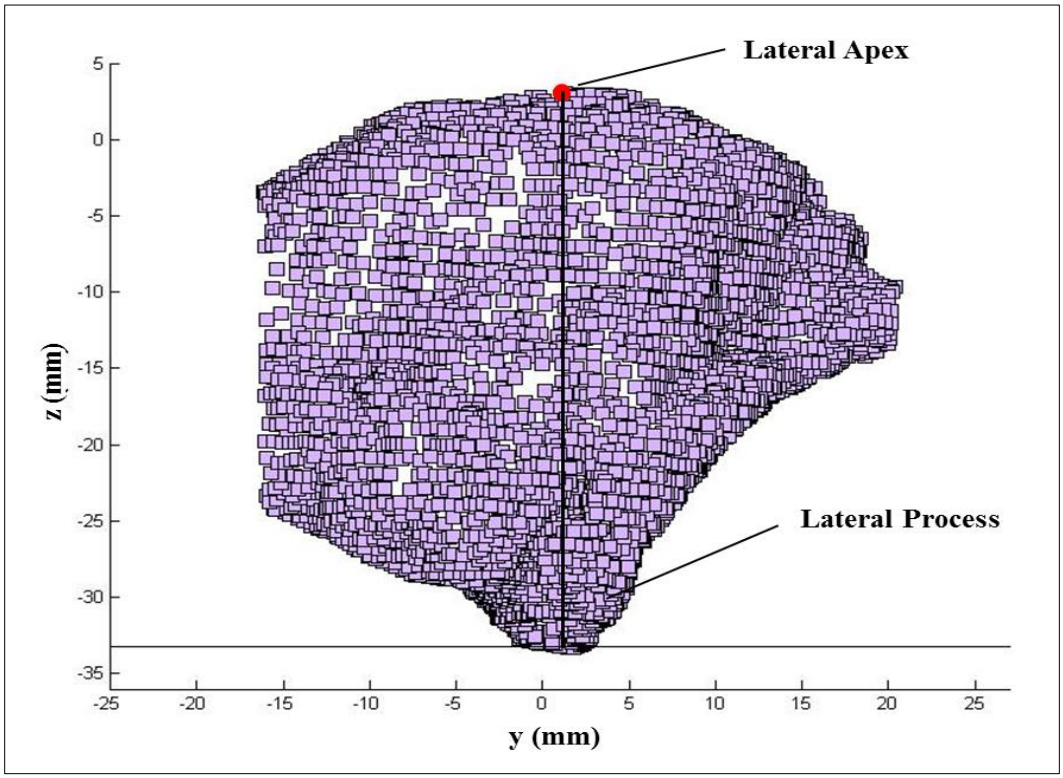

Figure 10 Calculation of the lateral height.

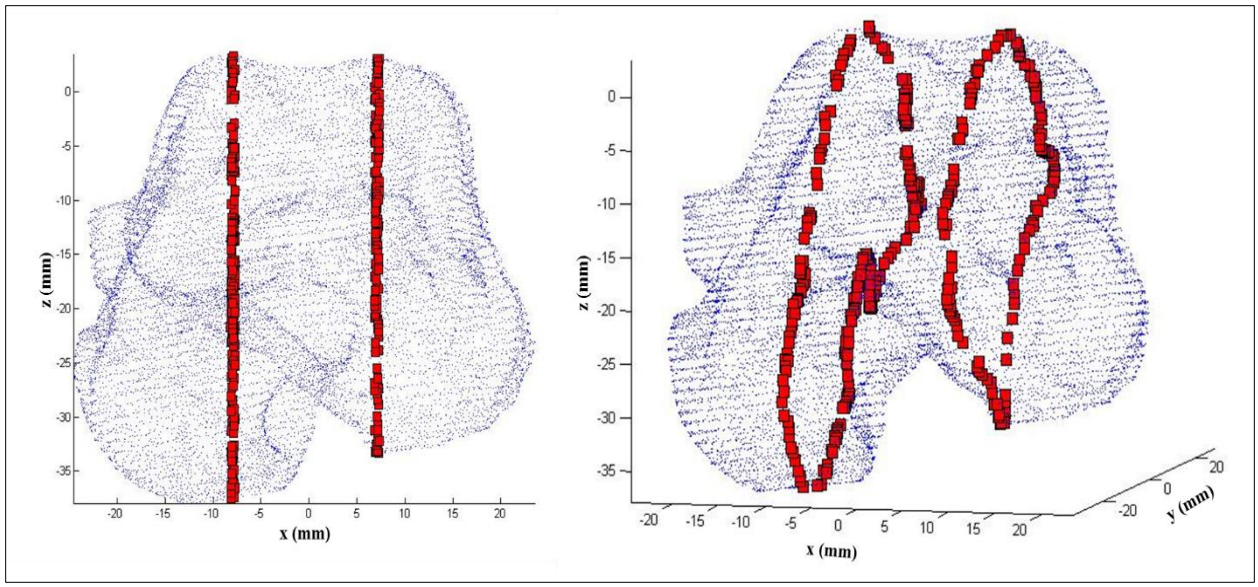

Figure 11 Identification of reference points in sagittal planes to create medial and lateral facets for use in calculating radius of curvature.

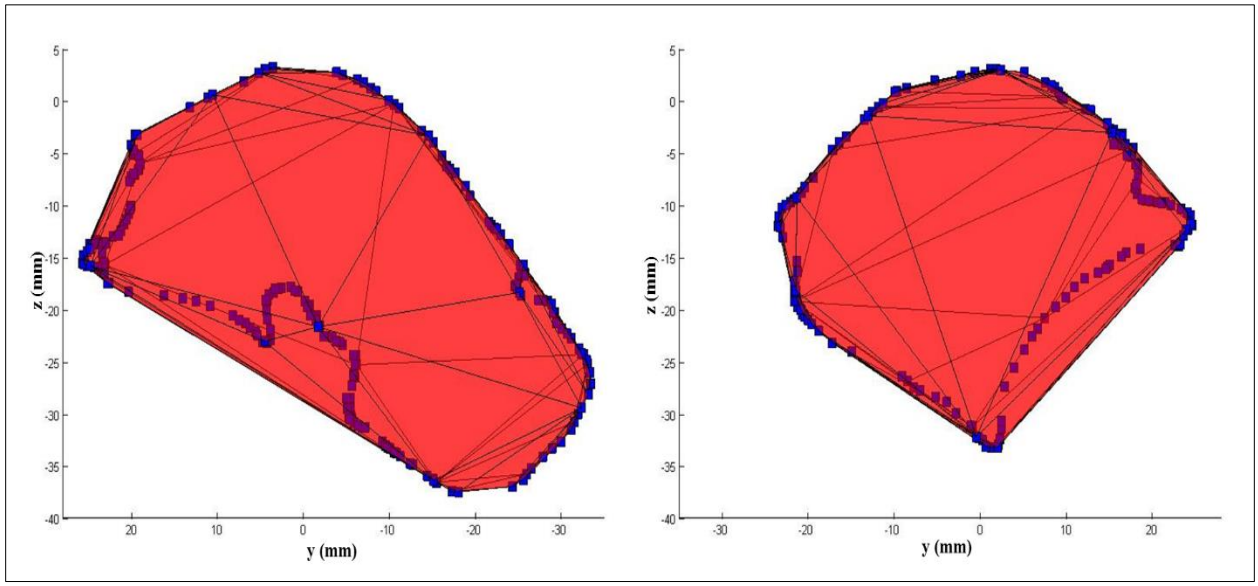

Figure 12 Convex hull applied to facets of the sagittal planes. a) Convex hull of medial facet. b) Convex hull of lateral facet.

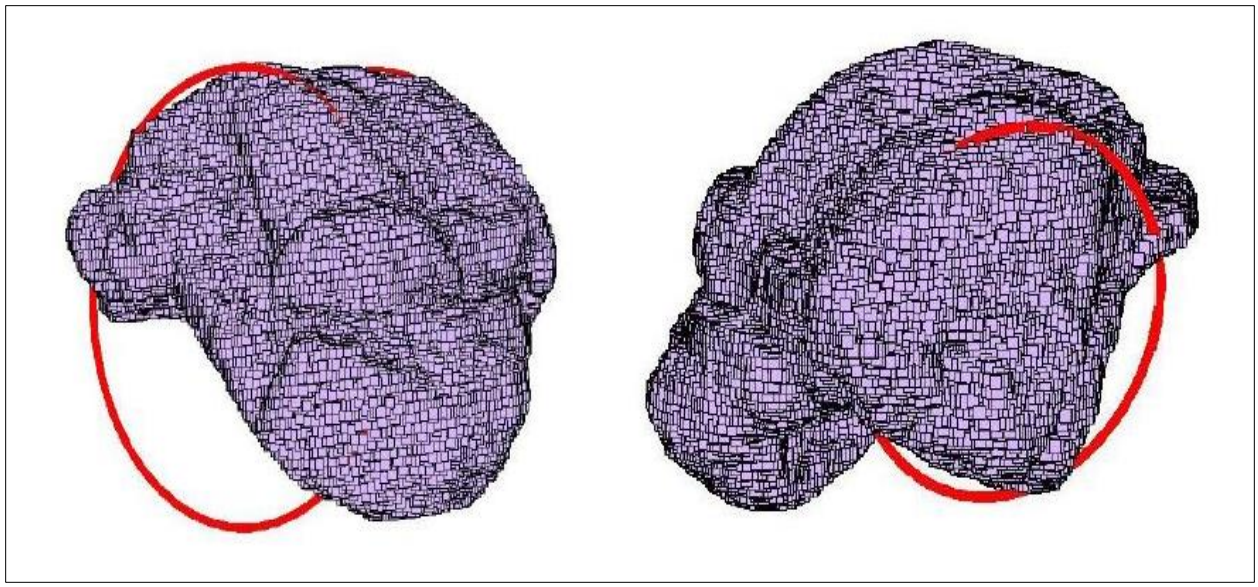

Figure 13 Visual representation of the radius of curvature of the talus. a) Medial radius of curvature. b) Lateral radius of curvature.

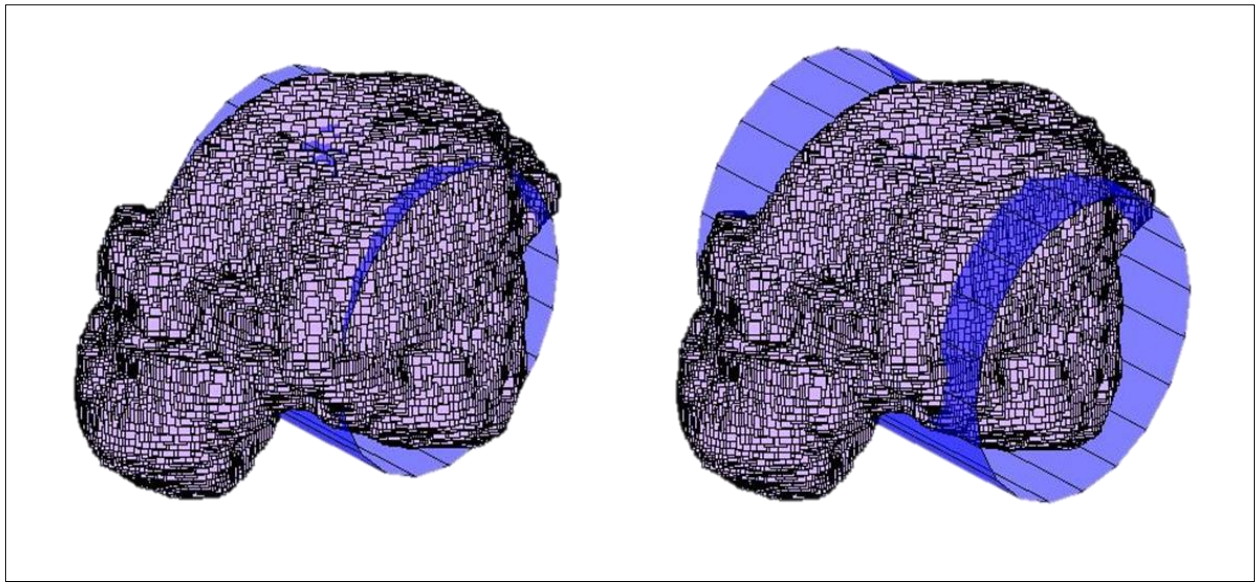

Figure 14 Model of cylindrical volume. a) Cylindrical volume of the talar body. b) Cylindrical volume of the talus.

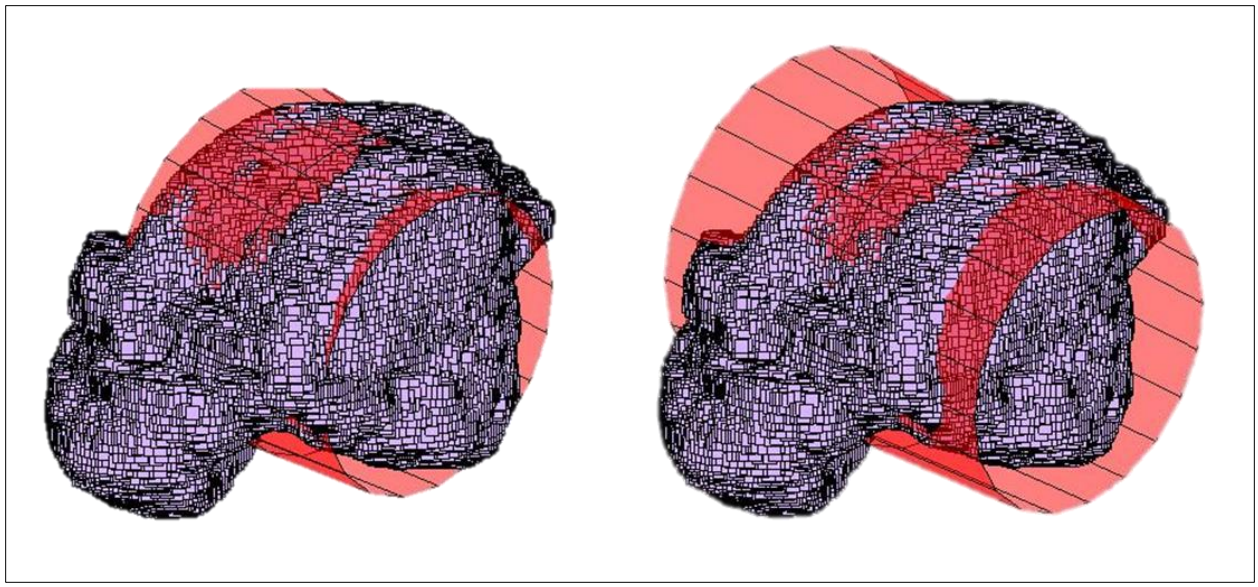

Figure 15 Model of truncated cone volume. a) Truncated cone volume of the talar body. b) Truncated cone volume of the talus.

3.2.5 Statistical Analysis

Statistical analysis was carried out using SPSS statistical tool package (IBM, Armonk, New York). Significance level was set to alpha = 0.05 for all statistical tests. Means and standard deviations were calculated for every parameter studied. Normality was tested using Shapiro-Wilk test. All studied parameters exhibited normal distribution. Two-way ANOVA ($p = 0.05$) and LSD post-hoc test were used to evaluate gender, side, group (healthy, OA), and KL grade differences.

3.3 Results

All study parameters were compared with respect to gender, anatomical side, study group (OA vs. non-OA), and KL grade. Results for each parameter are shown in Tables 2-9.

3.3.1 Medial Radius

Average medial radius (MR) for all subjects was 22.23±1.94 mm. There was a significant difference between gender; male subjects had an average medial radius of 23.12±1.01 mm, whereas female subjects averaged 20.27±1.04 mm ($p<0.0001$).

There were no significant differences between the medial radii of different anatomical sides (22.51±1.64 vs. 22.04±2.11, p=0.3314). Additionally, there were no differences between study group (p=0.1556), and there were no differences seen among different KL grades (p=0.5032).

3.3.2 Lateral Radius

Average lateral radius (LR) was 18.28±3.00 mm. The osteoarthritic group exhibited significantly larger radii compared to the non-arthritic group (p<0.0001). There were also significant differences seen between varying KL grades (p=0.0003). Male subjects had an average lateral radius larger than female subjects (17.03±1.20 vs. 15.38±1.38, p=0.0058). There were no significant differences seen between left and right ankles (p=0.8099).

3.3.3 Medial Height

The average medial height (MH) of all subjects was 27.52±3.58 mm. The medial height of male subjects on average were larger than female subjects (28.21±3.65 vs. 25.63±2.32, p=0.0587). However, there were no other significant differences exhibited between left and right ankles (p=0.30007), between healthy and OA groups (p=0.3764), and between KL grades (p=0.9269).

3.3.4 Lateral Height

Average lateral height (LH) was 35.05±3.92 mm. There were significant differences seen between genders (p<0.0001). There were no significant differences between left and right ankles (p=0.8354), but there were differences between healthy and OA groups (p=0.1321) and between KL grades (p=0.1457).

3.3.5 Cylindrical Volume

The average cylindrical volume (CV) for the talar body was 34,362.46±13,305.13 mm^3. There were significant differences seen between gender (p=0.0001), between study groups (p=0.001), and between KL grades (p=0.0198). The volume of the talar body was larger in males

than in females (31,316.33±5,553.16 vs. 22,605.91±2,571.96). Volume of the body appears to significantly increase in the appearance of OA (38,048.58±14,469.59 vs. 27,150.48±6,182.08).

The average cylindrical volume for the talus was 52,277.87±22,107.54 mm^3. Like the cylindrical volume of the body, the talus exhibited significant differences between male and female subjects ($p<0.0001$), between OA and non-OA subjects ($p=0.0013$), and between KL grades ($p=0.02$).

3.3.6 Truncated Cone Volume

The average truncated cone volume (TCV) of the talar body was 44,245.38±12,743.31 mm^3. There were significant differences observed between gender ($p<0.0001$), between study group ($p=0.0015$), and between varying KL grades ($p=0.0302$).

The average truncated cone volume of the talus was 66,976.40±21,124.58 mm^3. There were significant differences seen between gender ($p<0.0001$), between study groups ($p=0.0022$), and between KL grades ($p=0.0363$).

Table 2 Results for medial radius (MR).

Medial Radius (mm)				
Parameter		**Mean**	**SD**	**P-value**
Gender	F	20.27	1.04	**<0.0001**
	M	23.12	1.01	
Side	L	22.51	1.64	0.3314
	R	22.04	2.11	
Group	OA	22.46	1.99	0.1556
	Non-OA	21.76	1.77	
KL	1	21.85	1.76	0.5032
	2	23.06	2.34	
	3	22.51	1.95	
	4	21.95	2.16	

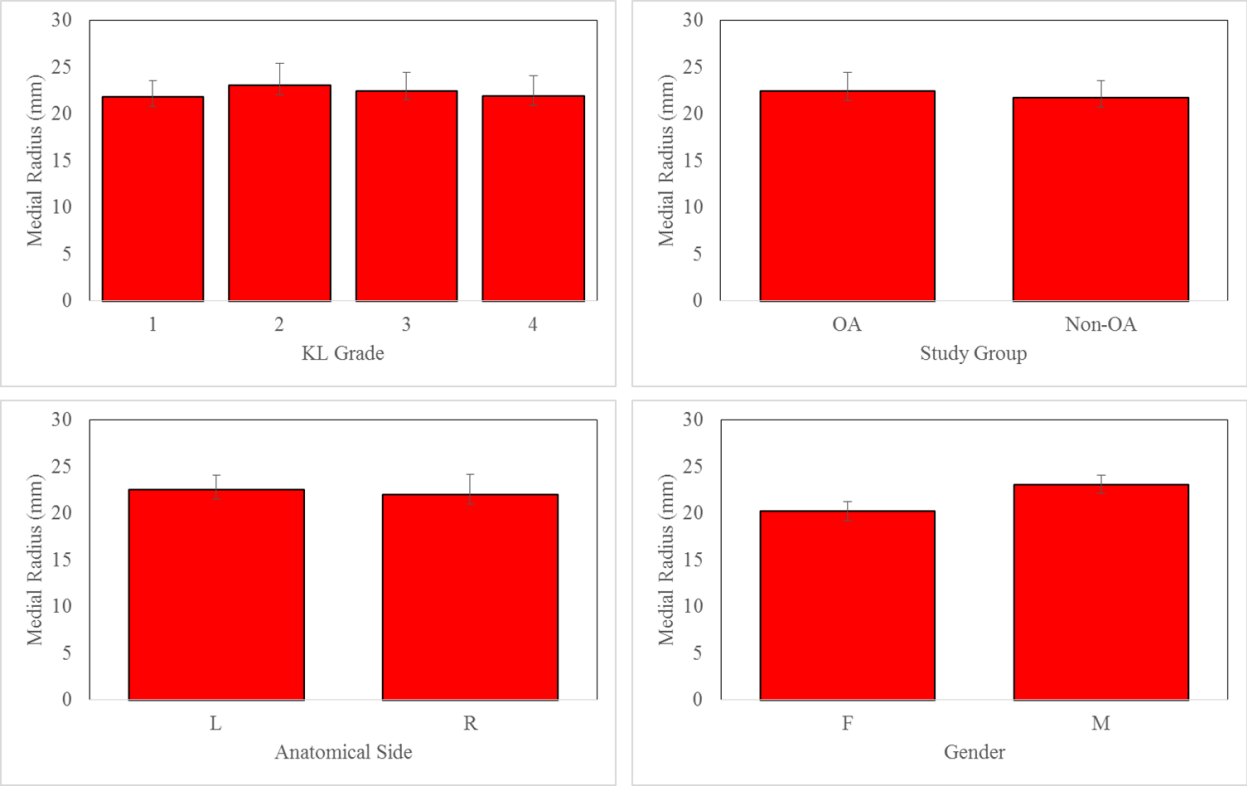

Figure 16 Statistical evaluation of MR±SD. a) MR by KL grade. b) MR by study group. c) MR by anatomical side. d) MR by gender.

Table 3 Results for lateral radius (LR).

Lateral Radius (mm)				
Parameter		**Mean**	**SD**	**P-value**
Gender	F	15.38	1.38	**0.0058**
	M	17.03	1.20	
Side	L	18.17	2.74	0.8099
	R	18.35	3.19	
Group	OA	19.32	3.04	**<0.0001**
	Non-OA	16.24	1.52	
KL	1	16.23	1.55	**0.0003**
	2	20.53	3.52	
	3	19.49	2.97	
	4	18.44	3.18	

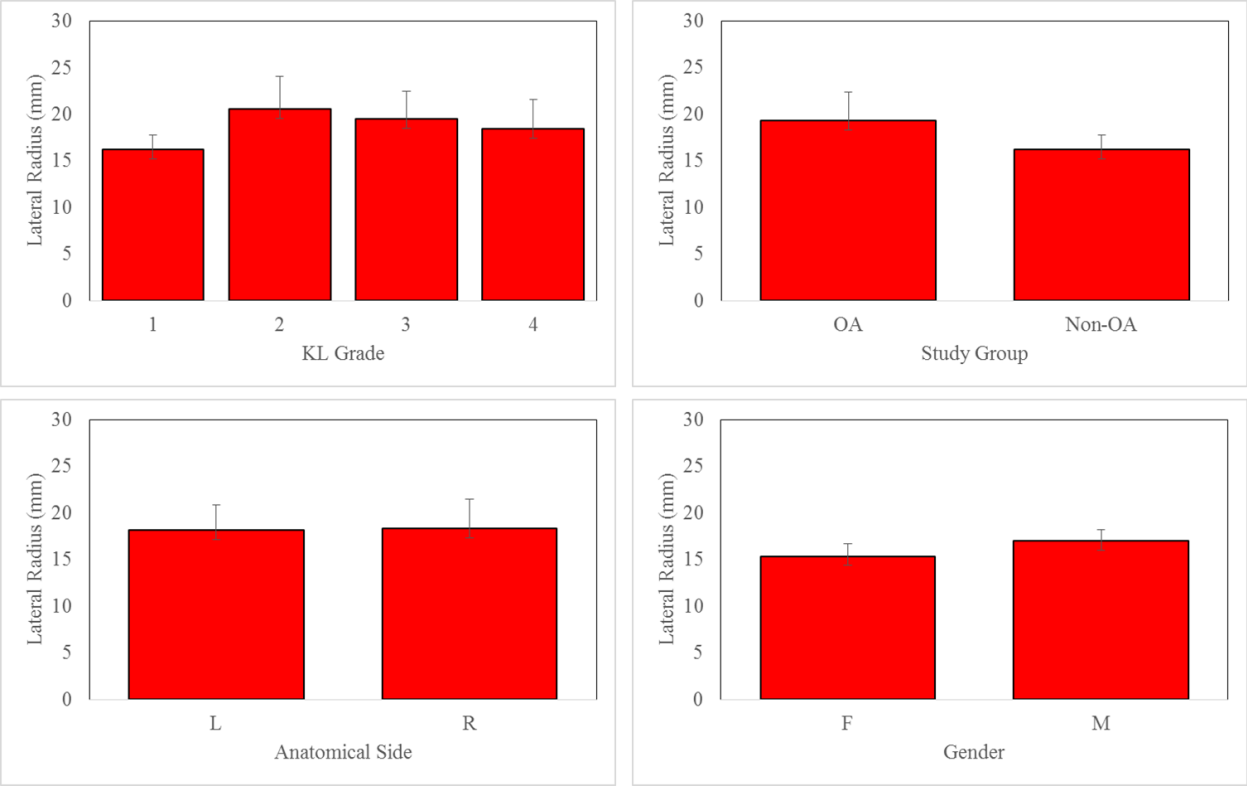

Figure 17 Statistical evaluation of LR±SD. a) LR by KL grade. b) LR by study group. c) LR by anatomical side. d) LR by gender.

Table 4 Results for medial height (MH).

Medial Height (mm)				
Parameter		**Mean**	**SD**	**P-value**
Gender	F	25.63	2.32	0.0587
	M	28.21	3.65	
Side	L	28.08	3.82	0.3007
	R	27.15	3.41	
Group	OA	27.80	3.73	0.3764
	Non-OA	26.98	3.29	
KL	1	27.13	3.29	0.9269
	2	27.90	3.05	
	3	27.81	3.74	
	4	27.43	4.24	

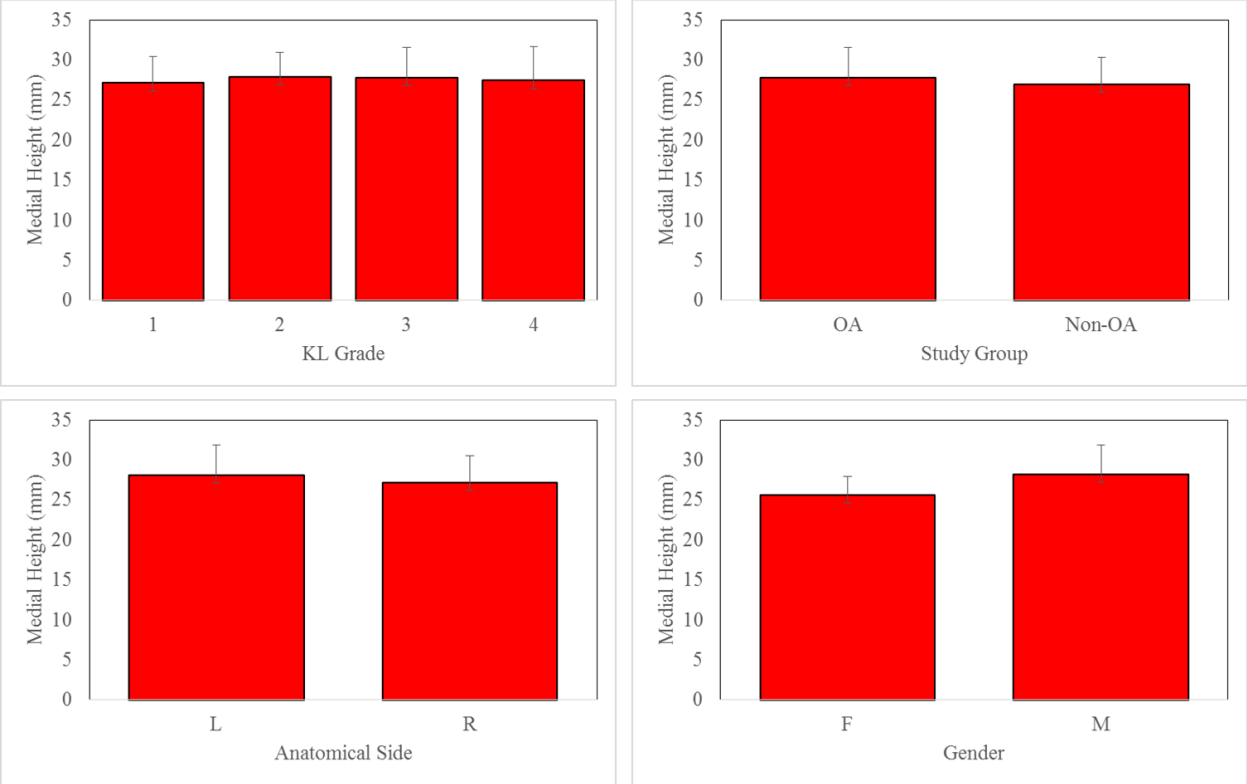

Figure 18 Statistical evaluation of MH±SD. a) MH by KL grade. b) MH by study group. c) MH by anatomical side. d) MH by gender.

Table 5 Results for lateral height (LH).

Lateral Height (mm)				
Parameter		**Mean**	**SD**	**P-value**
Gender	F	31.99	1.75	**<0.0001**
	M	35.94	1.88	
Side	L	34.93	3.14	0.8354
	R	35.14	4.39	
Group	OA	35.57	4.35	0.1321
	Non-OA	34.05	2.69	
KL	1	34.14	2.72	0.1457
	2	36.43	3.03	
	3	36.28	4.37	
	4	33.97	4.43	

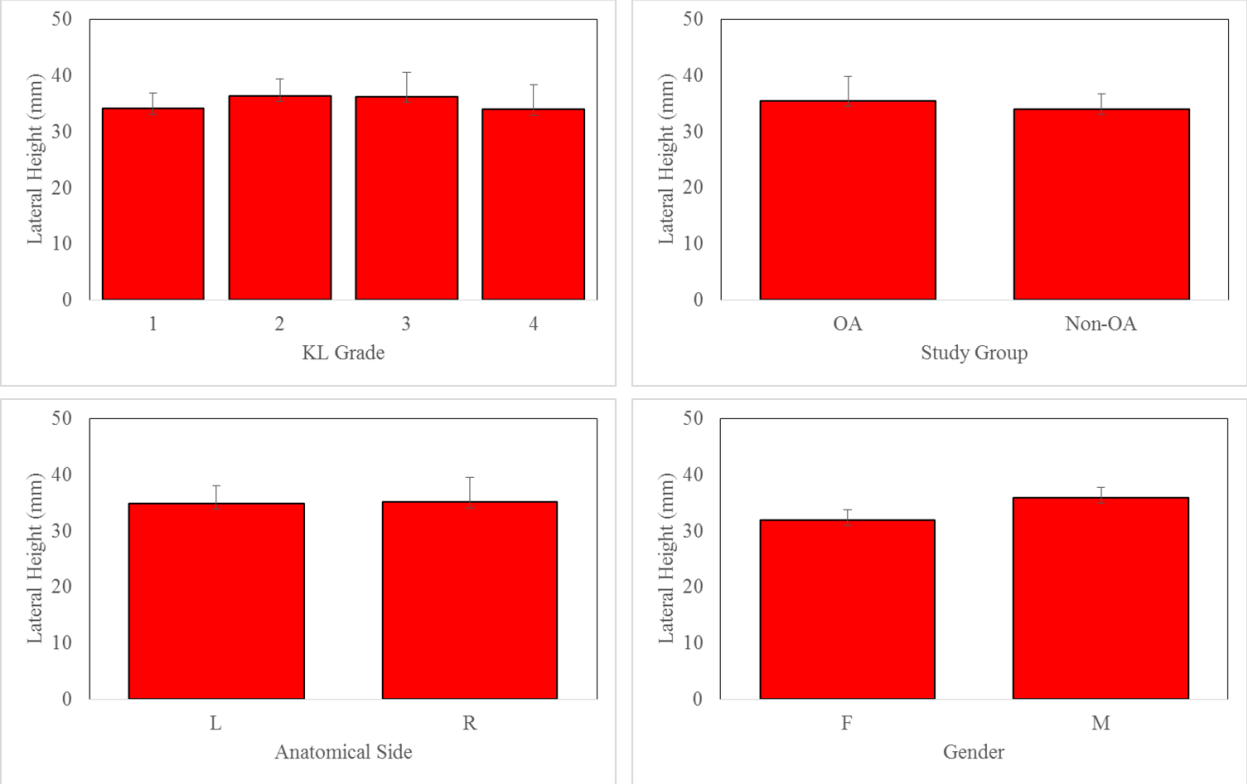

Figure 19 Statistical evaluation of LH±SD. a) LH by KL grade. b) LH by study group. c) LH by anatomical side. d) LH by gender.

Table 6 Results for cylindrical volume of the talar body (CV).

Cylindrical Body Volume (mm^3)				
Parameter		**Mean**	**SD**	**P-value**
Gender	F	22,605.91	2,571.96	**0.0001**
	M	31,316.33	5,553.16	
Side	L	33,636.44	11,867.95	0.7179
	R	34,840.56	14,296.07	
Group	OA	38,048.58	14,469.59	**0.0010**
	Non-OA	27,150.48	6,182.08	
KL	1	27,214.09	6,319.86	**0.0198**
	2	37,035.50	9,148.96	
	3	38,606.44	14,723.20	
	4	36,546.43	16,236.20	

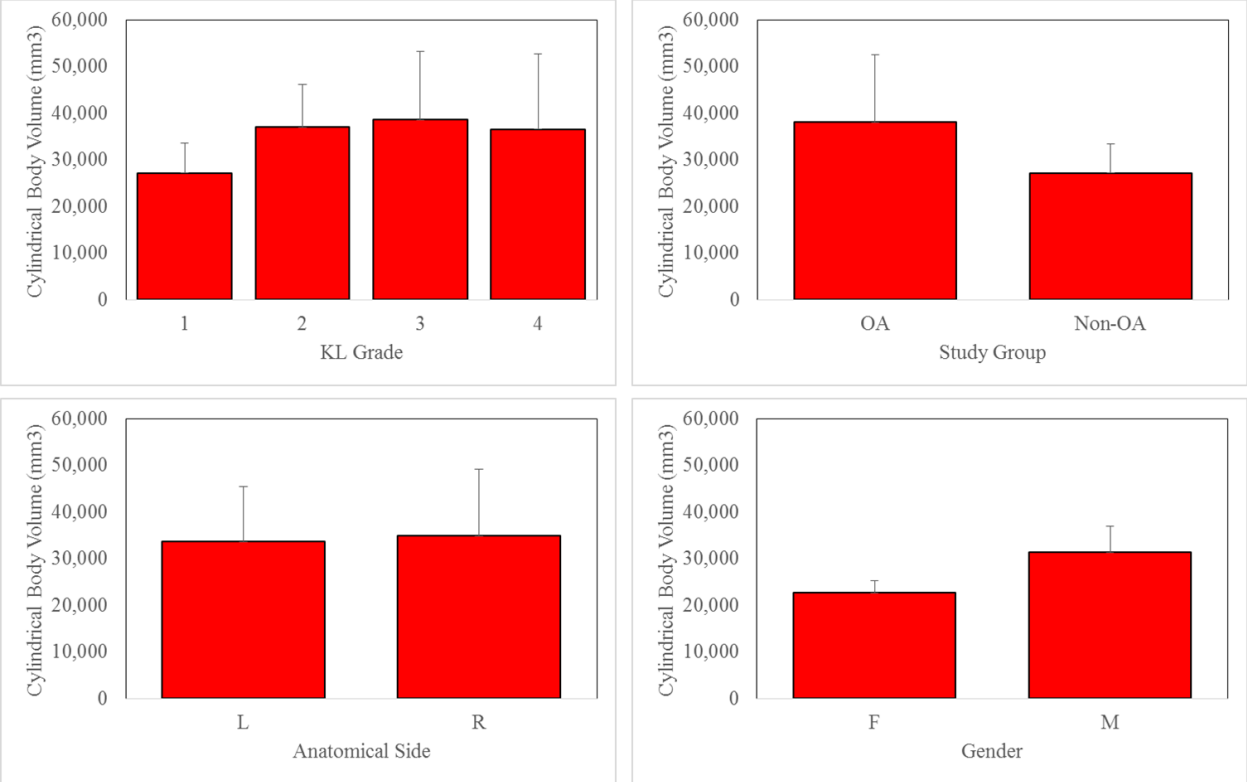

Figure 20 Statistical evaluation of CV of talar body±SD. a) CV of talar body by KL grade. b) CV of talar body by study group. c) CV of talar body by anatomical side. d) CV of talar body by gender.

Table 7 Results for cylindrical volume (CV).

Cylindrical Volume (mm^3)				
Parameter		**Mean**	**SD**	**P-value**
Gender	F	33,064.82	3,925.03	**<0.0001**
	M	47,472.25	8,460.60	
Side	L	51,025.78	20,239.55	0.7077
	R	53,102.41	23,465.39	
Group	OA	58,255.89	24,242.39	**0.0013**
	Non-OA	40,581.74	9,845.98	
KL	1	40,572.77	10,077.58	**0.0200**
	2	53,944.00	14,600.19	
	3	59,391.41	24,515.00	
	4	56,941.36	27,188.23	

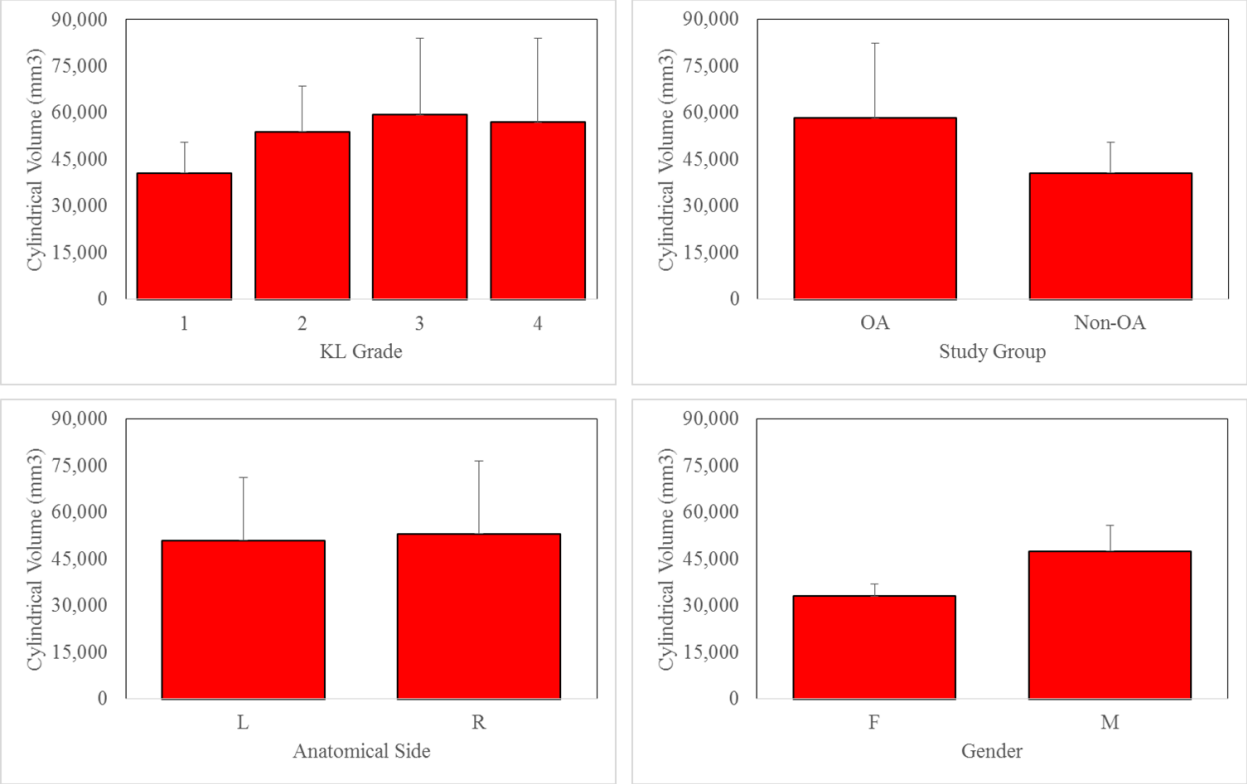

Figure 21 Statistical evaluation of CV±SD. a) CV by KL grade. b) CV by study group. c) CV by anatomical side. d) CV by gender.

Table 8 Results for truncated cone volume of the talar body (TCV).

Truncated Cone Body Volume (mm^3)				
Parameter		**Mean**	**SD**	**P-value**
Gender	F	30,931.36	1,537.28	**<0.0001**
	M	43,670.17	5,449.86	
Side	L	44,411.78	11,369.42	0.9311
	R	44,135.80	13,709.64	
Group	OA	47,653.31	13,528.95	**0.0015**
	Non-OA	37,577.70	7,632.68	
KL	1	37,868.73	7,680.57	**0.0302**
	2	49,281.50	12,259.83	
	3	48,198.74	13,740.13	
	4	44,589.21	14,646.01	

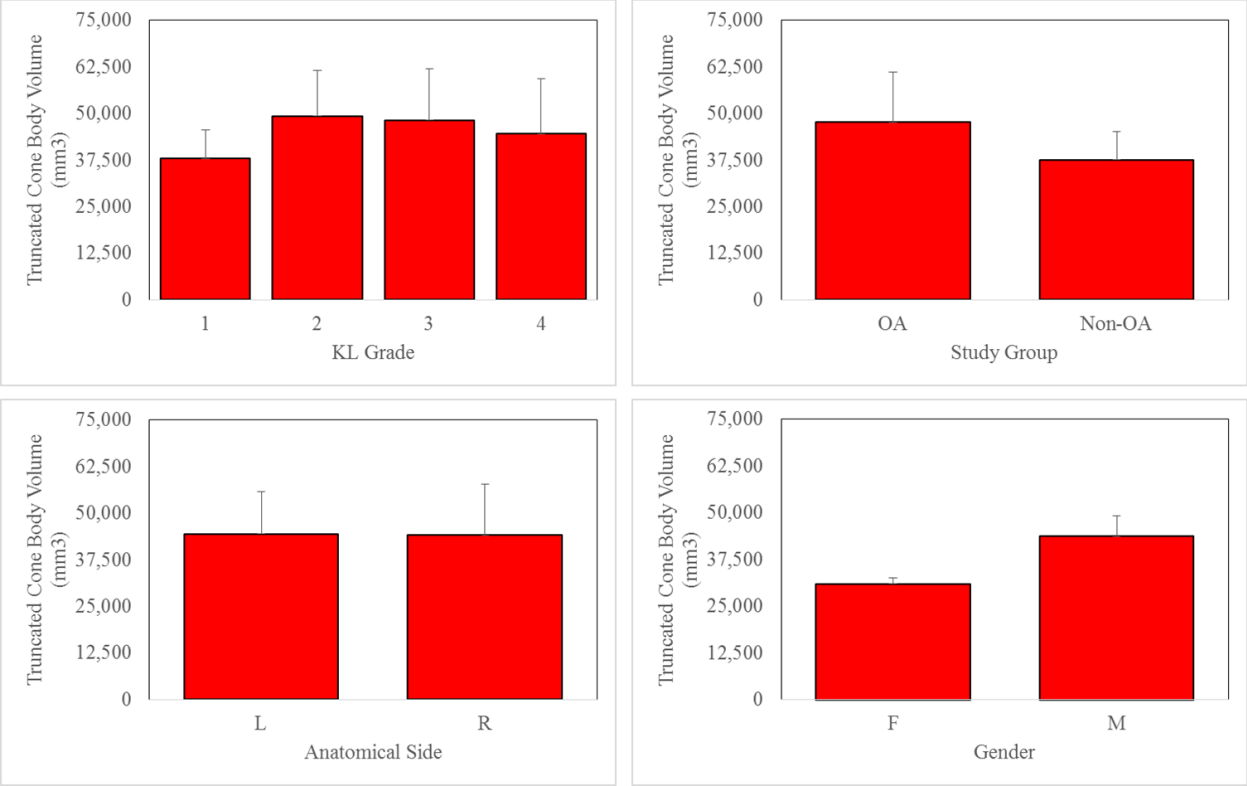

Figure 22 Statistical evaluation of TCV of talar body±SD. a) TCV of talar body by KL grade. b) TCV of talar body by study group. c) TCV of talar body by anatomical side. d) TCV of talar body by gender.

Table 9 Results for truncated cone volume (TCV).

Truncated Cone Volume (mm^3)				
Parameter		**Mean**	**SD**	**P-value**
Gender	F	45,421.82	4,931.22	**<0.0001**
	M	66,168.50	8,159.49	
Side	L	66,886.89	18,165.76	0.9776
	R	67,035.34	23,085.92	
Group	OA	72,460.73	22,588.79	**0.0022**
	Non-OA	56,246.17	12,515.05	
KL	1	56,558.82	12,717.30	**0.0363**
	2	71,239.50	17,257.98	
	3	73,746.19	22,456.63	
	4	69,028.07	25,928.84	

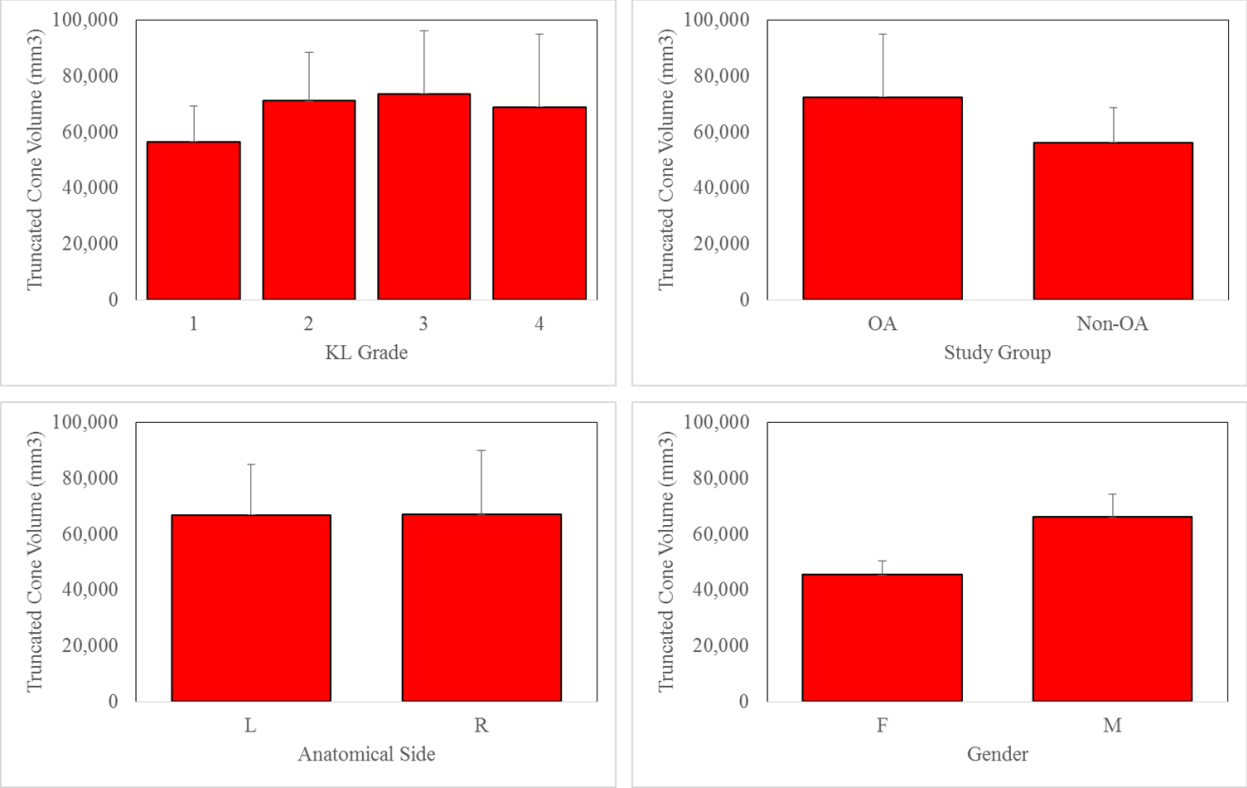

Figure 23 Statistical evaluation of TCV±SD. a) TCV by KL grade. b) TCV by study group. c) TCV by anatomical side. d) TCV by gender.

CHAPTER 4: DISCUSSION

4.1 Comparison of Results with Previous Literature

Refer to Appendix B for a direction comparison between the results from selected previous studies and the results of this study.

The most recent study done by Wiewiorski et al. is one of the only studies to address morphological differences between both osteoarthritic and non-pathologic ankles [6]. The study done by Wiewiorski et al., similar to the current study, shows comparable differences between the radii of OA tali and the radii of normal tali, which provides evidence of flattening that occurs due to degeneration. Wiewiorski et al. additionally measured the talar dome radius at the midsagittal plane and found the difference between groups to be more significant compared to medial and lateral measurements. Their method for evaluating the radius is based solely on the curvature of the talar dome, whereas this study evaluates the entire talus. This difference could explain the nominal variation in results. The current study shows a more significant difference in lateral radius between OA and normal subjects. The pattern seen in height differences are conflicting because of the different methods used for calculations. In the current study, the medial and lateral heights are evaluated for the entire length of the talus, while Wiewiorski et al. measures height of the talar dome calculated from its transverse plane to the highest points in the medial and lateral sagittal planes. However, in their method they experienced a statistically significant difference in height between the OA and control group, while the current study did not. Another study that assessed morphometry of pathologic ankles was done by Hayes et al. [5]. This study was not as innovative

as the study done by Wiewiorski et al. because only osteoarthritic ankles were examined. Hayes et al. used CT scans without converting them to 3D models to evaluate parameters of the talus. Measurements of the radius were done by evaluating points identified directly on the images. Unlike the current study, measurements were not done automatically by use of computational methods. Hayes et al. sought to evaluate the radius of the midsagittal section of the talus only. However, their findings that the radius was larger in males compared to females were consistent with the current study.

Previous three-dimensional studies, such as studies done by Wiewiorski et al. [21], Siegler et al. [20], and Kuo et al. [19], examine the geometry of non-pathologic ankles. The methods for calculating radius was similarly completed between the studies by Wiewiorski et al. and by Kuo et al. In both studies, the radius of curvature was based on the curve of the talar dome. There were no statistical significances between the medial and lateral radii in either studies. On the other hand, Siegler et al. conducted calculations of the radius similarly to the current study. Siegler et al. evaluated the radius of curvature established by sagittal facets calculated from the entire talus. The research shows a significant difference between the medial and lateral talar curves ($p<0.05$) [20].

A study done by Stagni et al. evaluated morphometry using two-dimensional techniques [4]. Like the majority of other morphometric studies, Stagni et al. evaluated the radius of curvature by referencing the talar dome instead over using the entire talus. Results revealed gender differences consistent with other studies as well as the current study. Similar to the methods used by Hayes et al., Stagni et al. did not rely on automatic approaches developed by computational methods. However, the calculations done were not fully reliant on an operator, only the initial reference points were manually selected.

4.2 Implications of Study

Ankle joint OA is a degenerative disease that affects morphology and morphometry of the talus and the mortise formed by distal tibia and fibula. Disputable signs of OA include changes in joint space, bone density and bone size (hypertrophy). Available surgical treatment of end-stage OA includes total ankle joint replacement or arthrodesis, both of which result in severe limitations. Despite the fact that OA is a slow, insidious process that is likely amenable to remission early in the process, little has been done to identify an early signs of OA progression.

This current work is, to the best of our knowledge, the first to report on 3D morphometric parameters of the talus at all 4 stages of OA progression (KL grades). Results showed that talar morphometry is gender specific and is independent of anatomical side. Medial talar height was significantly different in the OA group and at differing KL grades, while the measure of the lateral talar height did not show significant differences between healthy and OA group and between individual KL grades. This may be an indicator of the uneven flattening of the talus. On the other hand, both lateral and medial radii of curvature of the talar dome were significantly larger in the OA group, confirming previously published work.

The use of CT scans in three-dimensional evaluation of the morphometry of the talus has become more favorable to previous studies that have relied on radiographic methods. A 3D analysis presents greater information regarding geometric and volumetric data of the ankle. While more studies are increasingly promoting the use of 3D analysis, there are only a few that focus on progressive anatomical changes caused by osteoarthritis. Assessing the morphometry of the ankle as it undergoes degenerative changes is an important tool in clinical assessment and intervention. Not only will assessment reveal more information on the etiology of ankle OA, it will also provide

more information regarding progression at every stage and aid in prosthesis design for joint arthroplasty.

A comparative analysis of a healthy and an osteoarthritic talus shows that there is visual evidence of longitudinal flattening and transverse widening. These changes are supported by the current study, which confirms that average lateral radii is significantly larger in osteoarthritic ankles. The 2016 study done by Wiewiorski et al. [6] presented similar results, supporting curvature changes in the presence of OA. However, what previous studies lack overall is the ability to support changes of the ankle at varying degrees of osteoarthritis progression [19, 21]. To our knowledge, this is the first study to evaluate 3D morphology at differing KL grades, representing the disease's progression.

By comparing morphometric changes among varying KL grades, we are able to assess specific geometric markers of the talus related to its severity, independent of radiographic observation. Radiographic assessment may not always reveal implicative characteristics of degeneration until patients enter the end-stages of the disease. We will eventually be able to measure progressive trends alongside each stage of the disease in the hopes to translate this information to imaging studies. These parameters identified by automatic imaging evaluation allows for better and earlier clinical intervention. By identifying early signs of degeneration, clinicians will have a better opportunity to provide conservative treatment options and prevent further joint destruction. While the etiology and pathophysiology of ankle OA are still largely unknown, clinical representations of increased pain and tenderness can be associated by radiographic evidence of bony alterations. Diagnosing OA at early stages in order to identify and assess bony deformations with the aim of treating OA and decreasing joint paint may be possible by using imaging methods. By creating a computerized element, we are able to extract additional

information that may not be able to be seen with current radiographic methods. These specific identifiers will possibly be able to decrease the incidence of end-stage ankle OA by allowing clinicians to recognize early signs of the disease, and therefore apply conservative treatment to prevent further degeneration. This could ultimately reduce the need for surgical intervention, which has not been able to produce positive, long-term patient outcomes thus far. The goals of arthroplasty and arthrodesis are to eliminate pain, however, these methods may produce increased risks of complication, failure, and need for revision surgery. Assessing OA at the earliest stage possible could give a better insight on the cause and accumulation of morphological change, and may intervene with degeneration before needing surgical treatment.

An important implication of this study is that there is strong inclination that the lateral side of the ankle is more susceptible to morphological changes, possibly driven by osteoarthritis. The structure of the talus shows that the head and neck are positioned more medially on the body. Along with the difference in medial and lateral curvature of the talar dome, the asymmetry of the talus could relate to the lateral-focus changes seen in osteoarthritis.

Current surgical interventions appear to be problematic. There are high failure rates associated with arthroplasty, and fusion tactics limit motion and functionality. Ankle prosthesis have been designed using the morphometry of healthy ankles, which ultimately may cause problems due to the absence of integration of geometric changes seen in OA. The goals of several previous studies have been to assess the compatibility of ankle prosthesis in relation to its geometry.

The KL classification of osteoarthritis has limitations, due to the fact that it relies on the observer. Using an automatic imaging study in conjunction with radiographic assessment can allow clinicians to assess OA more effectively and efficiently. One requirement of OA

classification is narrowing of the joint space. This parameter can be quantified and evaluated against the grading scale, providing more information regarding the degenerative process.

4.3 Study Limitations

Being a preliminary study, our work has limitations. First, using a total of 68 subjects made it difficult to match a cohort to every evaluated group. While we can speculate that the leg overcomes a cycle of increased instability followed by stabilization, having only four subjects representing KL grade 2 may have impacted parameterization. Second, the retrospective nature of the study limited inclusion of the patients with no pathology in their lower extremity. Patients who did not exhibit any or limited presence of OA were in fact patients treated at the orthopaedic clinic for a trauma non-related to the talus bone. One may question whether those patients exhibit the geometrical characteristics of the healthy individual. Third, only small number of talar-specific geometric parameters (height and radius) were included for us to be able to postulate the etiology of ankle osteoarthritis. Fourth, the average age of the OA group was relatively higher than the average age of the normal group. Age bias could affect assessment of age-related degeneration. Additionally, because it is speculated that post-menopausal women experience changes to bone metabolism that affect their susceptibility to degeneration, age and gender limitations of our cohort made assessment of this etiologic subgroup difficult. However, we believe this work will serve as a base for the further research. We aim to include more parameters and the evaluation of the tibial mortise in the future.

CHAPTER 5: CONCLUSION

5.1 Contributions to the Field

This current study contributes the field by assessing how ankle morphometry changes at each stage of osteoarthritis progression. From the results, we are able to see that the changes of the talus are a function of OA progression. The evaluation and quantification of this progression can help better assess presence of OA at earlier stages, hopefully decreasing the prevalence of end-stage OA requiring surgical intervention. With respect to previous morphometric analysis of the ankle joint, the present study reports on a more detailed aspect of degenerative disease and takes into account the changes that occur overtime. While morphology cannot precisely relate to pathology, we are able to discover more information about osteoarthritis by more closely identifying specific parameters and markers that are characteristic of the disease at earlier stages.

Current radiographic techniques used for assessment are more often using 3D imaging, which reveals more information about surrounding tissues. This study utilizes volumetric information obtained from imaging. An automatic method for assessment could serve as a diagnostic tool to more accurately analyze degenerative diseases, such as osteoarthritis. Such a tool would be able to identify information not easily seen by an observer. Proper implication of the tool could coincide with improving current classification standards, which are known to have complications.

5.2 Future Work

All future work should be built on the foundation established in this work. Increasing the study population, particularly patients with KL grade 2, would allow us to better assess the progressive trends at each stage. In addition to the parameters presented in this thesis, it would be advisable to add parameters focusing on the tibial mortise and parameters concentrating on the relationship (e.g. congruence) between the talus and the tibia. Other than morphometric parameters, the evaluation of the combined effects of morphology (subchondral bone density distribution) and localized cartilage thickness would be of a value especially when etiology of OA is of interest. The existence of the relationship between geometric parameters, structural parameters (SBDD) and cartilage thickness estimated for individual articulating members (talus, distal tibia) would help not only in explaining the OA progression, and design of ankle arthroplasty, but rather aid surgeons in diagnosis and treatment of ankle pathology.

REFERENCES

1. Nakamura, Y., et al., *Bone alterations are associated with ankle osteoarthritis joint pain.* Sci Rep, 2016. **6**: p. 18717.

2. Saltzman, C.L., et al., *Epidemiology of ankle arthritis: report of a consecutive series of 639 patients from a tertiary orthopaedic center.* Iowa Orthop J, 2005. **25**: p. 44-6.

3. Valderrabano, V., et al., *Etiology of ankle osteoarthritis.* Clin Orthop Relat Res, 2009. **467**(7): p. 1800-6.

4. Stagni, R., et al., *Ankle morphometry evaluated using a new semi-automated technique based on X-ray pictures.* Clin Biomech (Bristol, Avon), 2005. **20**(3): p. 307-11.

5. Hayes, A., Y. Tochigi, and C.L. Saltzman, *Ankle morphometry on 3D-CT images.* Iowa Orthop J, 2006. **26**: p. 1-4.

6. Wiewiorski, M., et al., *Computed Tomographic Evaluation of Joint Geometry in Patients With End-Stage Ankle Osteoarthritis.* Foot Ankle Int, 2016. **37**(6): p. 644-51.

7. Murphy, L. and C.G. Helmick, *The impact of osteoarthritis in the United States: a population-health perspective.* Am J Nurs, 2012. **112**(3 Suppl 1): p. S13-9.

8. Nelson, A.E. and J.M. Jordan, *171 - Osteoarthritis: Epidemiology and classification A2 - Hochberg, Marc C*, in *Rheumatology (Sixth Edition)*, A.J. Silman, et al., Editors. 2015, Content Repository Only!: Philadelphia. p. 1433-1440.

9. Chambers, S., J. Ramaskandhan, and M. Siddique, *Radiographic Severity of Arthritis Affects Functional Outcome in Total Ankle Replacement (TAR).* Foot Ankle Int, 2016. **37**(4): p. 351-4.

10. Valderrabano, V., et al., *Gait analysis in ankle osteoarthritis and total ankle replacement.* Clin Biomech (Bristol, Avon), 2007. **22**(8): p. 894-904.

11. LaMothe, J., et al., *Analysis of Total Ankle Arthroplasty Survival in the United States Using Multiple State Databases.* Foot Ankle Spec, 2016. **9**(4): p. 336-41.

12. Guyer, A.J. and G. Richardson, *Current concepts review: total ankle arthroplasty.* Foot Ankle Int, 2008. **29**(2): p. 256-64.

13. Easley, M.E., et al., *Total ankle arthroplasty.* J Am Acad Orthop Surg, 2002. **10**(3): p. 157-67.

14. Huch, K., K.E. Kuettner, and P. Dieppe, *Osteoarthritis in ankle and knee joints.* Semin Arthritis Rheum, 1997. **26**(4): p. 667-74.

15. Lohmander, L.S. and H.P. Roos, *Osteoarthritis*, in *Textbook of Sports Medicine*. 2008, Blackwell Science Ltd. p. 422-434.

16. Braun, H.J. and G.E. Gold, *Diagnosis of osteoarthritis: imaging.* Bone, 2012. **51**(2): p. 278-88.

17. Eger, W., et al., *Human knee and ankle cartilage explants: catabolic differences.* J Orthop Res, 2002. **20**(3): p. 526-34.

18. Leardini, A., *Geometry and mechanics of the human ankle complex and ankle prosthesis design.* Clin Biomech (Bristol, Avon), 2001. **16**(8): p. 706-9.

19. Kuo, C.C., et al., *Three-dimensional computer graphics-based ankle morphometry with computerized tomography for total ankle replacement design and positioning.* Clin Anat, 2014. **27**(4): p. 659-68.

20. Siegler, S., et al., *The Clinical Biomechanics Award 2013 -- presented by the International Society of Biomechanics: new observations on the morphology of the talar dome and its relationship to ankle kinematics.* Clin Biomech (Bristol, Avon), 2014. **29**(1): p. 1-6.

21. Wiewiorski, M., et al., *Computer tomographic evaluation of talar edge configuration for osteochondral graft transplantation.* Clin Anat, 2012. **25**(6): p. 773-80.

22. Brockett, C.L. and G.J. Chapman, *Biomechanics of the ankle.* Orthop Trauma, 2016. **30**(3): p. 232-238.

23. Moore, K.L.a., et al., *Essential clinical anatomy*. Fifth edition. ed. 2015, Philadelphia: Wolters Kluwer Health.

24. Baums, M.H., et al., *Cartilage repair techniques of the talus: An update.* World J Orthop, 2014. **5**(3): p. 171-9.

25. Donatelli, R.A., *Normal biomechanics of the foot and ankle.* J Orthop Sports Phys Ther, 1985. **7**(3): p. 91-5.

26. Treppo, S., et al., *Comparison of biomechanical and biochemical properties of cartilage from human knee and ankle pairs.* J Orthop Res, 2000. **18**(5): p. 739-48.

27. van Dijk, C.N., et al., *Osteochondral defects in the ankle: why painful?* Knee Surg Sports Traumatol Arthrosc, 2010. **18**(5): p. 570-80.

28. Kuettner, K.E. and A.A. Cole, *Cartilage degeneration in different human joints.* Osteoarthritis Cartilage, 2005. **13**(2): p. 93-103.

29. Buckwalter, J.A., et al., *The Roles of Mechanical Stresses in the Pathogenesis of Osteoarthritis: Implications for Treatment of Joint Injuries.* Cartilage, 2013. **4**(4): p. 286-294.

30. Akkiraju, H. and A. Nohe, *Role of Chondrocytes in Cartilage Formation, Progression of Osteoarthritis and Cartilage Regeneration.* J Dev Biol, 2015. **3**(4): p. 177-192.

31. Aigner, T., N. Schmitz, and D.M. Salter, *175 - Pathogenesis and pathology of osteoarthritis A2 - Hochberg, Marc C*, in *Rheumatology (Sixth Edition)*, A.J. Silman, et al., Editors. 2015, Content Repository Only!: Philadelphia. p. 1462-1476.

32. Felson, D.T. and Y. Zhang, *172 - Local and systemic risk factors for incidence and progression of osteoarthritis A2 - Hochberg, Marc C*, in *Rheumatology (Sixth Edition)*, A.J. Silman, et al., Editors. 2015, Content Repository Only!: Philadelphia. p. 1441-1446.

33. Maleki-Fischbach, M. and J.M. Jordan, *New developments in osteoarthritis. Sex differences in magnetic resonance imaging-based biomarkers and in those of joint metabolism.* Arthritis Res Ther, 2010. **12**(4): p. 212.

34. Price, M.D. and C.P. Chiodo, *Chapter 49 - Foot and Ankle Pain A2 - Firestein, Gary S*, in *Kelley and Firestein's Textbook of Rheumatology (Tenth Edition)*, R.C. Budd, et al., Editors. 2017, Elsevier. p. 734-741.

35. Cracchiolo III, A., *Ankle arthrodesis*, in *Atlas Foot and Ankle Surgery, Second Edition*. 2005, CRC Press. p. 345-359.

36. Altman, R.D. and M.C. Hochberg, *181 - Management of osteoarthritis*, in *Rheumatology (Sixth Edition)*. 2015, Content Repository Only!: Philadelphia. p. 1508-1514.

37. Barton, T., F. Lintz, and I. Winson, *Biomechanical changes associated with the osteoarthritic, arthrodesed, and prosthetic ankle joint.* Foot Ankle Surg, 2011. **17**(2): p. 52-7.

38. Valderrabano, V., et al., *Kinematic changes after fusion and total replacement of the ankle: part 3: Talar movement.* Foot Ankle Int, 2003. **24**(12): p. 897-900.

39. Hintermann, B. and V. Valderrabano, *Ankle joint replacement*, in *Atlas Foot and Ankle Surgery, Second Edition*. 2005, CRC Press. p. 361-367.

APPENDIX A: PROTOCOL

A.1 Three-Dimensional CT Model Segmentation Protocol

Program: Materialized MIMICS 14.2

Procedure:

1. To convert CT scan from DICOM
    a. Go to Mimics 14.12
    b. File: Import images
    c. Select all files
    d. Add Auto
    e. Unselect compression
    f. Select desired target directory to create a new project
    g. Convert
2. File: Open CT scans
3. Set Threshold levels (determine visually)
4. Record selected threshold
5. Select Edit
    a. Erase unwanted pixels
    b. Set color for masks
        i. Need to color each slice containing talus
        ii. Color perimeter of the talus cortex
        iii. "Fill" the area inside the perimeter
6. Go to Project Manager
    a. Select desired mask
    b. Use Calculate 3D to get pixel coordinates
    c. Visually inspect 3D model
7. Export point-cloud and volumetric model

Figure A1 Procedure on how to segment three-dimensional models from CT scans using Materialized MIMICS software.

A.2 Talar Dome Surface Model Segmentation Protocol

Program: Eraser CT (custom-written C++)

Procedure:

1. Open Eraser CT program
2. Click open file button
3. Select folder containing desired subject talus surface point-cloud
4. Click X button
5. Adjust orientation of the talus RX-, RX+, RY-, RY+, RZ-, RZ+ buttons such that talus is oriented in the sagittal view
6. Click draw button
7. Draw portion of talar dome that represent outer surface
8. Click drawSave button and enter the FILENAME1
9. Open file and select drown surface FILENAME1
10. Adjust orientation using RX-, RX+, RY-, RY+, RZ-, RZ+ buttons such that talar dome is in the top view
11. Click erase button and remove unnecessary points if needed
12. Click eraseSave button and enter the FILENAME2

Figure A2 Procedure on how to segment talar dome surface using the custom-written program Eraser CT.

APPENDIX B: RESULTS COMPARED WITH PREVIOUS STUDIES

Table B1 Radius of curvature calculated in current study compared to previous studies.

Parameter	Anatomical Location	Grouping		Wiewiorski [6]*	Wiewiorski [21]*	Siegler [20]	Kuo [19]*	Hayes [5]*	Stagni [4]*	Current Study
Radius (mm)	Medial	OA	All	22.9±3.1						22.5±1.2
			Female							
			Male							
		Normal	All	19.9±2.4	20.4±2.5	25.7±4.8	21.8±3.0			21.7±1.8
			Female				20.6±3.0			
			Male				22.3±2.8			
	Midsagittal/ Center	OA	All	24.0±2.7				20.7±2.6		
			Female							
			Male							
		Normal	All	20.1±1.8	20.7±2.1	24.7±3.8	21.8±2.0		23.4±3.1	
			Female				21.6±2.0		21.1±1.9	
			Male				21.9±1.9		24.5±3.0	
	Lateral	OA	All	21.3±3.3						19.3±3.0
			Female							
			Male							
		Normal	All	19.4±2.5	20.3±2.0	21.7±2.9	20.9±3.0			16.3±1.5
			Female				21.4±3.0			
			Male				20.5±2.9			

Note: Asterisk (*) indicates that parameterization methods were different from the current study.

Table B2 Height calculated in current study compared to previous studies.

Parameter	Anatomical Location	Grouping		Wiewiorski [6]*	Kuo [19]*	Current Study
Height (mm)	Medial	OA	All	6.8±1.9		27.8±3.73
			Female			
			Male			
		Normal	All	8.0±2.2	11.9±1.83	26.98±3.29
			Female		11.8±2.0	
			Male		11.5±1.7	
	Lateral	OA	All	7.5±1.7		19.32±3.04
			Female			
			Male			
		Normal	All	8.6±2.9		16.24±1.52
			Female			
			Male			

Note: Asterisk (*) indicates that parameterization methods were different from the current study.

APPENDIX C: SAMPLE CODE

C.1 Talus Transformation

```
clear all
clc
%% import of point cloud, volume and surface
talusPC = dlmread('talusPC.txt');
talusHU = dlmread('talusHU.txt');
talusSURF = dlmread('talusSURF.txt');

%% Talus SBD code
% First step
% coordinate system

eigenTALUS = pca(talusSURF);

axisTALUS1 = eigenTALUS(:,1);
axisTALUS2 = eigenTALUS(:,2);
axisTALUS3 = eigenTALUS(:,3);

coordinateSystemTALUS = [axisTALUS1';axisTALUS2';axisTALUS3'];

centerTALUSsurf = mean(talusSURF);

%% Transformation to neutral axis using [cCS]
% local coordinate system
medialX = axisTALUS1;
medialY = axisTALUS2;
k = axisTALUS3;
% global coordinate system
ii = [1 0 0];
jj = [0 1 0];
kk = [0 0 1];

% translations
talusPCzeroed = [talusPC(:,1)-centerTALUSsurf(1,1),...
    talusPC(:,2)-centerTALUSsurf(1,2),...
    talusPC(:,3)-centerTALUSsurf(1,3),];
talusSURFzeroed = [talusSURF(:,1)-centerTALUSsurf(1,1),...
    talusSURF(:,2)-centerTALUSsurf(1,2),...
    talusSURF(:,3)-centerTALUSsurf(1,3),];

rotM=[medialX'*ii' medialX'*jj' medialX'*kk';
      medialY'*ii' medialY'*jj' medialY'*kk';
      k'*ii' k'*jj' k'*kk'];
```

Figure C1 Sample code used in methodology to automatically standardize and transform the models of the talus and the talar dome.

```
prompt = 'R or L ankle?: ';
str = input(prompt,'s');
str = upper(str);

if str == 'R'
    %inverting mediolateral axis
    sortedTalus = [sortedTalus(:,1)*-1,sortedTalus(:,2),sortedTalus(:,3)];
    sortedSurf = [sortedSurf(:,1)*-1,sortedSurf(:,2),sortedSurf(:,3)];
    %sort column by X
    sortedTalus = sortrows(sortedTalus,1);
    sortedSurf = sortrows(sortedSurf,1);
end


%% Transformation to global transverse plane
clc;

% minimum bounding box on talar dome surface
surfBox = boundingBox3d(sortedSurf);

dxSB = surfBox(2)-surfBox(1); % x distance
dySB = surfBox(4)-surfBox(3); % y distance
dzSB = surfBox(6)-surfBox(5); % z distance

% slicing x-axis in increments to make 50 planes
intSB = dxSB/50;

% extracting anterior points along talar dome surface
anteriorPts = [];
for a = surfBox(1):intSB:(surfBox(2)-intSB)
    range = sortedSurf(:,1)>=a & sortedSurf(:,1)<=(a+intSB);
    planeRange = sortedSurf(range,:);
    anteriorPts = [anteriorPts;planeRange(planeRange(:,2) ==
min(planeRange(:,2)),:)];
end
% removing outliers using 95 confidence interval
prctiles = prctile(anteriorPts(:,2),[5 95]);
outlierIndex = anteriorPts(:,2) < prctiles(1) | anteriorPts(:,2) >
prctiles(2);
anteriorPts(outlierIndex,:) = [];
% extracting posterior points along talar dome surface
posteriorPts = [];
for b = surfBox(1):intSB:(surfBox(2)-intSB)
    range = sortedSurf(:,1)>=b & sortedSurf(:,1)<=(b+intSB);
    planeRange = sortedSurf(range,:);
    posteriorPts = [posteriorPts;planeRange(planeRange(:,2) ==
max(planeRange(:,2)),:)];
end

% removing outliers
prctiles = prctile(posteriorPts(:,2),[5 95]);
outlierIndex = posteriorPts(:,2) < prctiles(1) | posteriorPts(:,2) >
prctiles(2);
posteriorPts(outlierIndex,:) = [];
```

Figure C1 (Continued)

```
% transverse plane fit from first and last anterior and posterior points
transversePlane =
fitPlane([anteriorPts(1,:);anteriorPts(end,:);posteriorPts(1,:);posteriorPts(
end,:)]);

% target plane in the global direction
% center not changed
target = [transversePlane(1) transversePlane(2) transversePlane(3) 1 0 0 0 1
0];

tform = createBasisTransform3d(transversePlane,target); % transform source
plane to target plane

sortedTalus = transformPoint3d(sortedTalus,tform);
sortedSurf = transformPoint3d(sortedSurf,tform);

sortedTalus = sortrows(sortedTalus,1);
sortedSurf = sortrows(sortedSurf,1);

% center points
centerTALUS = mean(sortedTalus);
centerTALUSsurf = mean(sortedSurf);
```

Figure C1 (Continued)

C.2 Identifying Medial and Lateral Apexes

```
%% Medial and Lateral Apexes

% median point of articular surface
mid = floor(size(sortedSurf,1)/2);

% medial surface
medialSurf = sortedSurf(1:mid,:);
% lateral surface
lateralSurf = sortedSurf(mid+1:end,:);

% MEDIAL
% extracting most superior points in medial surface
upperMedPts = [];
for c = floor(min(medialSurf(:,1))):1:floor(max(medialSurf(:,1))) % 1mm
sections
    range = medialSurf(:,1)>=c & medialSurf(:,1)<=(c+1); % all points in each
section
    maxpt = find(medialSurf(:,3) == max(medialSurf(range,3))); % most
superior point section
    upperMedPts = [upperMedPts;medialSurf(maxpt,:)];
end

upperMedPts = unique(upperMedPts,'rows'); % removing duplicate points

prctiles = prctile(upperMedPts(:,2),[5 95]); % removing outliers
outlierIndex = upperMedPts(:,2) < prctiles(1) | upperMedPts(:,2) >
prctiles(2);
upperMedPts(outlierIndex,:) = [];

upperMedPts = sortrows(upperMedPts,1);


medialApex = [];
for d = 1:size(upperMedPts,1)-1
    % testing points from lateral to medial, toward midpt
    if upperMedPts(d+1,3)>upperMedPts(d,3)
        medialApex = upperMedPts(d+1,:); % medial apex
    else
        break
    end
end


% LATERAL
% extracting most superior points in lateral surface
upperLatPts = [];
for e = floor(max(lateralSurf(:,1))):-1:floor(min(lateralSurf(:,1)))
    range = lateralSurf(:,1)>=e & lateralSurf(:,1)<=(e+1);
    maxpt = find(lateralSurf(:,3) == max(lateralSurf(range,3)));
    upperLatPts = [upperLatPts;lateralSurf(maxpt,:)];
end

upperLatPts = unique(upperLatPts,'rows'); % removing duplicate points

prctiles = prctile(upperLatPts(:,2),[5 95]); % removing outliers
outlierIndex = upperLatPts(:,2) < prctiles(1) | upperLatPts(:,2) >
prctiles(2);
```

Figure C2 Code for identifying the medial and lateral apexes of the talar dome surface.

```
upperLatPts(outlierIndex,:) = [];

upperLatPts = sortrows(upperLatPts,-1);


lateralApex = [];
for f = 1:size(upperLatPts,1)-1
    if upperLatPts(f+1,3)>upperLatPts(f,3)
        lateralApex = upperLatPts(f+1,:); % lateral apex
    else
        break
    end
end
```

Figure C2 (Continued)

C.3 Calculation of Radius of Curvature

```
%% Radius of curvature

% radius of an arc

% BASED ON TALUS BODY

% medial facet plane
medTalusFacet = find(sortedTalus(:,1)<=(medialApex(:,1)+0.25) &...
    sortedTalus(:,1)>=(medialApex(:,1)-0.25));
% lateral facet plane
latTalusFacet = find(sortedTalus(:,1)<=(lateralApex(:,1)+0.25) &...
    sortedTalus(:,1)>=(lateralApex(:,1)-0.25));

% medial polygonal area
mx = sortedTalus(medTalusFacet,2); my = sortedTalus(medTalusFacet,3);
mvi = convhull(mx,my);
marea = polyarea(mx(mvi),my(mvi));
mrad = sqrt(marea/pi());


% lateral polygonal area
lx = sortedTalus(latTalusFacet,2); ly = sortedTalus(latTalusFacet,3);
lvi = convhull(lx,ly);
larea = polyarea(lx(lvi),ly(lvi));
lrad = sqrt(larea/pi());
```

Figure C3 Code for calculating radius of curvature for the medial and lateral sections of the talus.

C.4 Calculation of Height

```
%% Medial and Lateral Height

talusBox = boundingBox3d(sortedTalus); % min bounding box on entire talus
surfBox = boundingBox3d(sortedSurf); % min bounding box on talar dome surface

% identifying talus body by using 'x' length of talar dome
talusBody = sortedTalus(sortedTalus(:,2)>=surfBox(3) &
sortedTalus(:,2)<=surfBox(4),:);

% reference plane by using median point, medial apex, lateral apex
centerRefPlane =
[sortedSurf(mid,1),sortedSurf(mid,2),sortedSurf(mid,3),0,0,1,0,1,0];
medialRefPlane = [medialApex,0,0,1,0,1,0];
lateralRefPlane = [lateralApex,0,0,1,0,1,0];

% MEDIAL
% extracting talus medial points that are on the medial side of the median
plane
medialPoints = [];
for h = 1:size(sortedTalus,1)
    testPoint = sortedTalus(h,:);
    testPointPlane = isBelowPlane(testPoint,centerRefPlane);
    if testPointPlane == 0
        medialPoints = [medialPoints;testPoint];
    else
        continue
    end
end

medialPoints = sortrows(medialPoints,2);

adjMedialPoints = medialPoints(find(medialPoints(:,3) ==
min(medialPoints(:,3))):end,:);
adjMedialPoints = sortrows(adjMedialPoints,3);

ptSet1 = adjMedialPoints(1:10,:);

adjMedialPoints = sortrows(adjMedialPoints,2);
ptSet2 = adjMedialPoints(end-9:end,:);

medialPlane = fitPlane([ptSet1;mean(ptSet2)]);
medialPlane = [medialPlane(1:3),1,0,0,medialPlane(4:6)];

medialHeight = distancePointPlane(medialApex,medialPlane);


% LATERAL

lateralPoints = [];
for h = 1:size(talusBody,1)
    testPoint = talusBody(h,:);
    testPointPlane = isBelowPlane(testPoint,lateralRefPlane);
    if testPointPlane == 1
        lateralPoints = [lateralPoints;testPoint];
```

Figure C4 Code for calculating the medial and lateral heights of the talus.

```
        else
            continue
        end
    end

    lateralPoints = sortrows(lateralPoints,3);
    lateralProcess = lateralPoints(1:5,:);
    lateralProcessPlane = [mean(lateralProcess),1,0,0,0,1,0];

    lateralHeight = distancePointPlane(lateralApex,lateralProcessPlane);
```

Figure C4 (Continued)

APPENDIX D: IRB EXEMPTION LETTER

UNIVERSITY OF SOUTH FLORIDA

RESEARCH INTEGRITY AND COMPLIANCE
Institutional Review Boards, FWA No. 00001669
12901 Bruce B. Downs Blvd., MDC035 • Tampa, FL 33612-4799
(813) 974-5638 • FAX (813) 974-7091

6/14/2017

Peter Simon
Orthopaedics & Sports Medicine
13020 N Telecom Parkway
Biomechanics Lab
Tampa, FL 33637

RE: **Not Human Subjects Research Determination**
IRB#: Pro00031214
Title: Morphometric Analysis of the Talus on the Cohort of Healthy and Arthritic Patient Population: In-Vivo 3D Computational Study

Dear Dr. Simon:

The Institutional Review Board (IRB) has reviewed your application. The activities presented in the application involve methods of program evaluation, quality improvement, and/or needs analysis. While potentially informative to others outside of the university community, study results would not appear to contribute to generalizable knowledge. As such, the activities do not meet the definition of research under USF IRB policy, and USF IRB approval and oversight are therefore not required.

While not requiring USF IRB approval and oversight, your study activities should be conducted in a manner that is consistent with the ethical principles of your profession. If the scope of your project changes in the future, please contact the IRB for further guidance.

If you will be obtaining consent to conduct your study activities, please remove any references to "research" and do not include the assigned Protocol Number or USF IRB contact information.

If your study activities involve collection or use of health information, please note that there may be requirements under the HIPAA Privacy Rule that apply. For further information, please contact a HIPAA Program administrator at (813) 974-5638.

Sincerely,

E. Verena Jorgensen, M.D., Chairperson
USF Institutional Review Board